Characterization of competitive oxidation reactions over a model Pt-Pd/Al$_2$O$_3$ diesel oxidation catalyst

by

Karishma Vistasp Irani

A thesis

presented to the University of Waterloo

in fulfilment of the

thesis requirement for the degree of

Master of Applied Science

in

Chemical Engineering

Waterloo, Ontario, Canada, 2009

AUTHOR'S DECLARATION

I hereby declare that I am the sole author of this thesis. This is a true copy of the thesis, including any required final revisions, as accepted by my examiners.

I understand that my thesis may be made electronically available to the public.

Karishma Irani

Abstract

There has been a growing interest in using lean-burn engines due to their higher fuel economy and associated lower CO_2 emissions. However, there are challenges in reducing NO_X in an O_2-rich (lean-burn) exhaust, and in low temperature soot oxidation. NO_X storage/reduction (NSR) and selective catalytic reduction (SCR) are commercial NO_X reduction technologies, and both are more efficient with levels of NO_2 that are higher than those that are in engine exhaust (engine-out NO_2 levels are ~10% of the total NO_X). Therefore diesel oxidation catalysts are installed upstream of these technologies to provide NO_2 through NO oxidation. The motivation behind this research project was two-fold. The first was to gain a better understanding of the effect of hydrocarbons on NO oxidation over a monolithic diesel oxidation catalyst. The second was to spatially resolve competitive oxidation reactions as a function of temperature and position within the same diesel oxidation catalyst (as that used in the first part). A technique known as spatially resolved capillary-inlet mass spectrometry (SpaciMS) was used to measure the gas concentrations at various positions within the catalyst.

Diesel engine exhaust contains a mixture of compounds including NO, CO and various hydrocarbons, which react simultaneously over a catalyst, and each can influence the oxidation rates of the others. While studying the effect of hydrocarbons on NO oxidation in this project, propylene was found to have an apparent inhibition effect on NO oxidation, which increased with increasing propylene concentration. This apparent inhibition is a result of the NO_2, as a product of NO oxidation, reacting with the propylene as an oxidant. Experiments with NO_2 demonstrate a significant temperature

decrease in the onset of NO_2 reduction when propylene was present, which decreased further with increasing amounts of propylene, verifying NO_2 as an oxidant. Similar results were observed with m-xylene and dodecane addition as well. The results also demonstrate that NO_2 was consumed preferentially relative to O_2 during hydrocarbon oxidation. With low inlet levels of O_2, it was evident that the addition of NO_2 had an apparent inhibition effect on propylene oxidation after the onset of NO_2 reduction. This subsequent inhibition was due to the NO formed, demonstrating that C_3H_6 results in reduced NO_2 outlet levels while NO inhibits C_3H_6 oxidation.

The development of new models as well as validation of existing models requires the ability to spatially resolve oxidation reactions within a monolith. Spatially-resolved data will also give catalyst manufacturers insight into the location of active fronts, thereby directing the design of more efficient catalysts. In this research project, spatially resolving the oxidation reactions demonstrated that H_2 and CO are oxidized prior to C_3H_6 and $C_{12}H_{26}$ and clearly show back-to-front ignition of the reductant species. An enhancement in NO oxidation was observed at the same time as dodecane oxidation light off, likely related to dodecane partial oxidation products.

Acknowledgments

I would like to express the deepest gratitude to my dearest parents, my brother, my fiancé Neville and the rest of my family. I would not have been able to achieve this without their love, guidance, support and encouragement.

I would also like convey my genuine gratitude to my supervisor Professor William Epling for his invaluable guidance and support throughout my study. His infinite patience and eagerness to help his students are only a couple of his immeasurable values which have helped me achieve this goal. Everything I have learnt from him will be treasured for the rest of my life.

In addition, I would like to express my appreciation to Professors João Soares and Flora Ng for their beneficial comments and precious time spent in reviewing this thesis.

I would also like to acknowledge helpful discussions with Richard Blint, Se Oh and Ed Bissett of the General Motors Research and Development Center.

Last but not least, I would like to thank all my colleagues and friends for their priceless help and support throughout this journey.

Dedication

To my dearest parents, my brother and my fiancé Neville

whose endless love, understanding, support and encouragement

helped make this possible.

Table of Contents

List of Figures

List of Tables

Chapter 1: Introduction

Over the last several years, there has been world-wide growing concern regarding air pollution effects on the environment and human health. This has led to significant focus on methods of reducing emissions into the atmosphere. One solution is using cleaner, more fuel-efficient engines. Current predictions suggest a shift to lean-burn engines for passenger vehicles from today's gasoline engines. One example of a lean-burn engine is the diesel engine. As compared to today's gasoline engines, diesel engines consume less fuel, resulting in better fuel economy, which is important considering all the recent fluctuations in fuel prices. A plot of fuel consumption versus vehicle weight is shown in Figure 1-1[1].
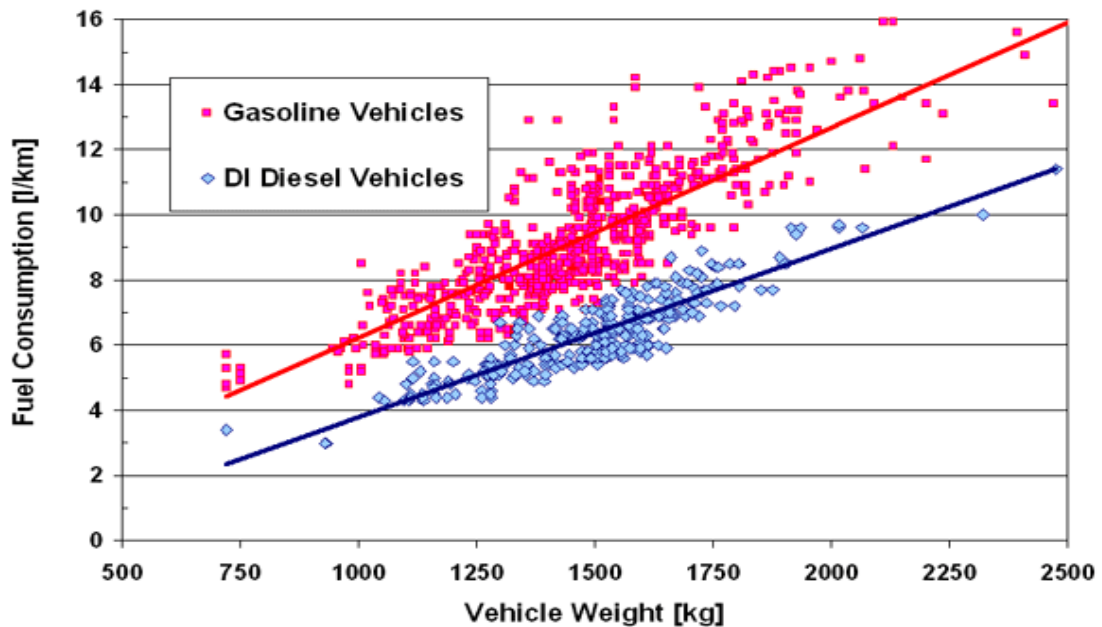
Figure 1-1: Comparison between gasoline- and diesel-powered vehicle fuel consumption

Due to decreased fuel consumption, diesel engines also release less CO_2 compared to gasoline vehicles. Figure 1-2 shows data obtained from a diesel vehicle,

producing CO_2 emissions which are 19% lower than those emitted from a gasoline vehicle of the same weight [2]. As mentioned earlier, diesels operate in a lean-burn mode, which means they have an air/fuel ratio that exceeds the stoichiometric amount required to just combust the fuel. Diesel exhaust therefore has excess oxygen, whereas today's gasoline engine exhaust is net-oxygen free. Gasoline engines can also be run in a lean-burn mode, but are currently not, due to the inability to control NO_X emissions.
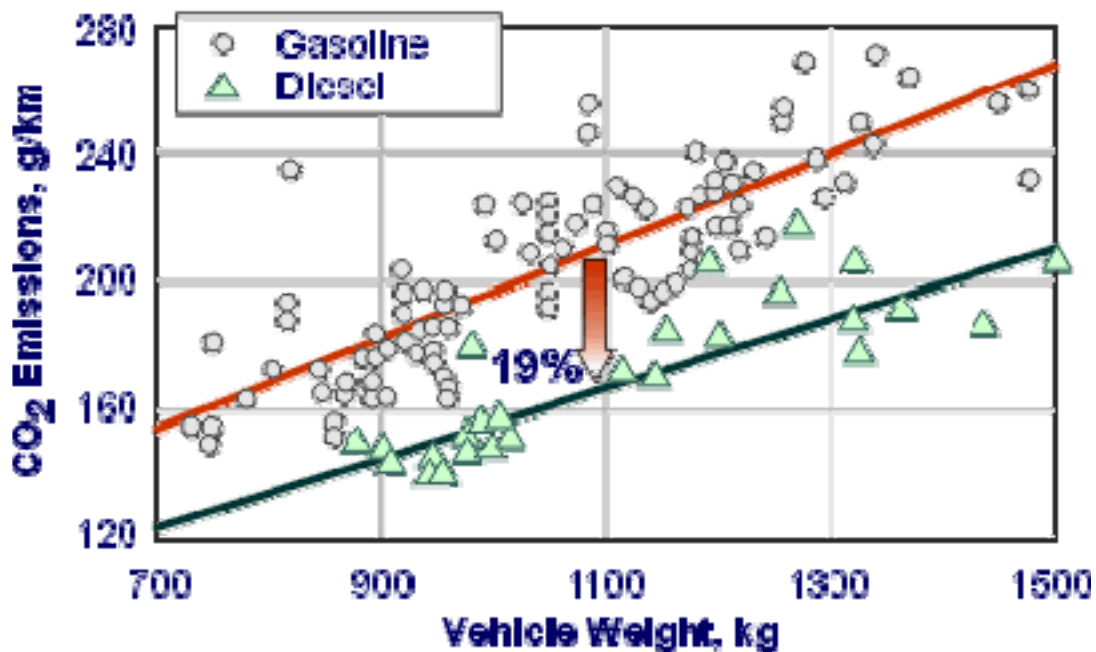
Figure 1-2: Comparison between gasoline- and diesel-powered vehicle CO_2 emissions

Vehicle emissions regulations target CO, hydrocarbon, NO_X and particulate matter emissions, and are becoming more stringent. Lower CO and hydrocarbon amounts are emitted from diesel engines, relative to gasoline; however reducing NO to N_2 in an oxygen-rich environment and oxidizing the particulate matter at normal exhaust temperatures are significant challenges.

Since its introduction in the 1980s, the three-way catalyst has helped lower NO_X emissions from stoichiometric-burn gasoline vehicles. However, this catalyst technology cannot be used to control NO_X from diesel or lean-burn engine exhaust because it is designed for exhaust conditions involving low, or net-free, O_2 concentrations and is inefficient when used in excess oxygen.

Currently, two catalyst systems have been proposed, and implemented, to reduce NO_X compounds to N_2 in lean-burn exhaust. The first involves the selective catalytic reduction (SCR) of NO_X to N_2 using ammonia, with urea as an ammonia precursor. The main chemical reactions that occur in this system are:

$$4NO + 4NH_3 + O_2 \leftrightarrow 4N_2 + 6H_2O \qquad (1)$$

$$2NO + 2NO_2 + 4NH_3 \leftrightarrow 4N_2 + 6H_2O \qquad (2)$$

Reaction (1) is called the "standard" reaction [3], while reaction (2), which involves the reduction of equi-molar concentrations of NO and NO_2 to N_2 by ammonia, is known to be faster than (1) [4]. SCR of NO_X to N_2 can also be achieved by using hydrocarbons from the exhaust gas as given by reaction (3) [5]. Such catalysts are called deNOx or lean NO_X catalysts (LNC).

$$\{HC\} + NO_X \leftrightarrow N_2 + CO_2 + H_2O \qquad (3)$$

However, this technology has not yet achieved commercial status as the conversions achieved are significantly lower relative to SCR by ammonia.

The second catalyst technology for NO_X reduction in diesel, or lean-burn, engines is NO_X storage/reduction (NSR) catalysis. In this system, NO_X is alternately stored, or

trapped, on the catalyst under normal, or lean, driving conditions and then this stored NO_X is reduced to N_2 during short phases which are rich in reductant such as hydrocarbons, CO or H_2. The trapping is done by either alkaline earth metals, such as Ba, or alkali metals, such as K [6].

Diesel exhaust is typically composed of 90 to 95% NO. During the lean phase which contains abundant O_2, NO is oxidized to NO_2. Then, the trapping components store NO_2 in the form of nitrates as shown in (4) [5].

$$BaO + 2NO_2 + 0.5O_2 \leftrightarrow Ba(NO_3)_2 \tag{4}$$

These nitrates become thermodynamically unstable under surplus fuel conditions or at higher temperatures and breakdown to either NO or NO_2 [7,8], as shown by reactions (5a) and (5b).

$$Ba(NO_3)_2 \leftrightarrow BaO + 2NO + 1.5O_2 \tag{5a}$$

$$Ba(NO_3)_2 \leftrightarrow BaO + 2NO_2 + 0.5O_2 \tag{5b}$$

Once the engine is switched to the rich or regeneration phase, the reductants such as hydrocarbons, CO or H_2 reduce the NO_X to N_2. Several studies have proposed that NO_2 is a precursor for, or at least an intermediate in, the trapping process [9-13] and can enhance the performance of the NSR catalyst by improving NO_X storage [14-20].

Diesel particulate filters (DPFs), or soot filters, capture solid particulates such as elemental carbon or soot from diesel exhaust and then intermittently oxidize them to gaseous CO_2 as given by reactions (6), (7) and (8). The soot oxidation reactions regenerate the filter and are required to remove the accumulated soot, which will

otherwise plug the filter over time, and/or cause high exhaust gas pressure drop, lowering the engine performance [5].

$$C + 0.5O_2 \leftrightarrow CO \tag{6}$$

$$NO_2 + C \leftrightarrow CO + NO \tag{7}$$

$$CO + 0.5O_2 \leftrightarrow CO_2 \tag{8}$$

The oxidation of carbon with oxygen is not easy, requiring temperatures on the order of 500 to 600°C. However, if NO_2 is used as the oxidant, the carbon can be burned at temperatures close to 350°C [21].

In evaluating the above technologies, including NO_2 in the feed enhances the performance of the SCR and NSR catalysts as well as helps regenerate soot filters. However, the engine-out amount of NO_2 is only 10% of the total NO_X [5]. So, to enhance these technologies, an upstream catalyst is typically installed, which is designed, amongst other things, to generate more NO_2. This catalyst is called a diesel oxidation catalyst (DOC).

As the name suggests, the DOC performs a range of oxidation functions by utilising the oxygen available in diesel exhaust. DOCs oxidize NO, CO and hydrocarbon emissions through the following oxidation reactions [5]:

$$NO + 0.5O_2 \rightarrow NO_2 \tag{9}$$

$$CO + 0.5O_2 \rightarrow CO_2 \tag{10}$$

$$HC + O_2 \rightarrow CO_2 + H_2O \tag{11}$$

The oxidation of CO and hydrocarbons are exothermic, thus heat is generated through reactions (10) and (11). The data shown in Figure 1-3 [22] demonstrate that NSR catalysts and SCR catalysts require temperatures between 300 to 450°C to optimize their NO_x conversion efficiencies. Thus, a DOC is designed to not only oxidize NO, but also to provide heat through exothermic hydrocarbon oxidation reactions. DOCs are usually installed upstream of the SCR and NSR catalysts, as well as the soot filters, for these reasons.
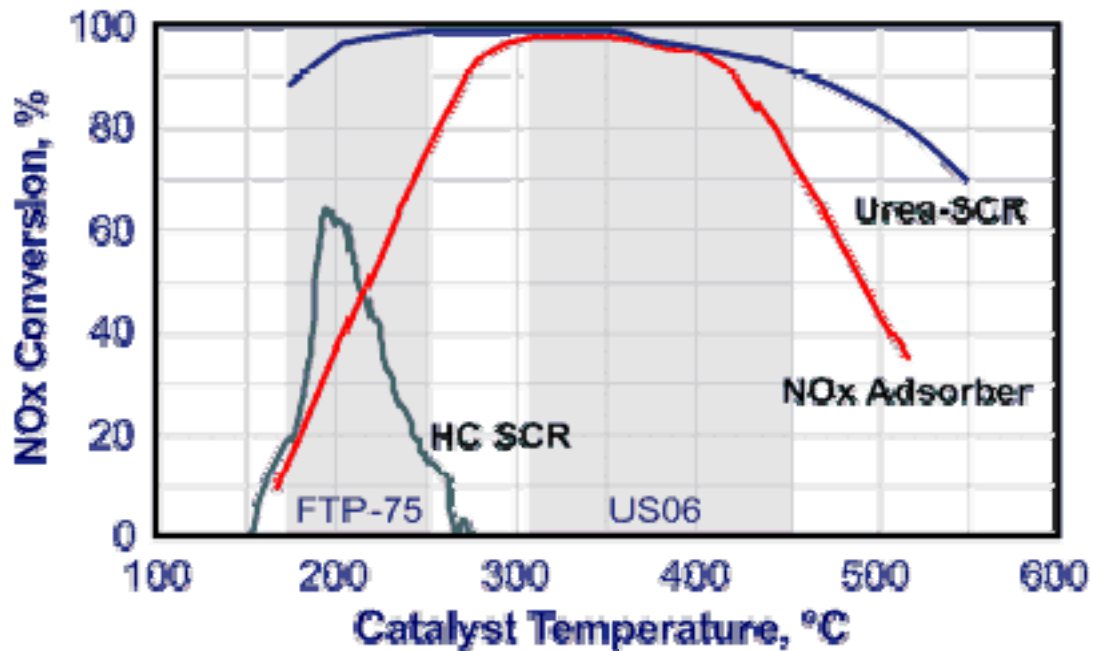
Figure 1-3: NO_x conversion using different catalyst technologies

There are a few vehicle manufacturers who have already implemented these emissions control technologies. For example, in 2003 Toyota launched a combined diesel particulate - NO_x reduction (DPNR) system with an upstream oxidation catalyst. Also, the 2007 diesel Dodge Ram heavy pickup truck includes an oxidation catalyst followed by a NSR catalyst and a catalyzed particulate filter. The Mercedes-Benz E320 Bluetec,

launched in 2006 in North America, has a combination of an oxidation catalyst and a NSR catalyst installed in the engine compartment followed by an underfloor particulate filter and an SCR catalyst. The 2009 BMW X5 xDrive35d and the 335d models have an oxidation catalyst and a diesel particulate filter, both housed in one unit, and an SCR catalyst with urea injection. The 2009 Volkswagen Jetta incorporates an oxidation catalyst placed upstream of a NSR catalyst as well as a diesel particulate filter to control the soot emissions. Honda has proposed the release of a diesel-powered Accord into the US market in 2009, with the exhaust clean-up including an oxidation catalyst and a particulate filter followed by a new double-layered NOx reduction catalyst, which combines a NSR catalyst with a SCR catalyst [23].

These commercial designs are not only proof of the growing popularity of diesel engines, but also demonstrate that DOCs are regularly installed upstream of the NSR and SCR catalysts and particulate filters, making them an integral part of an efficient exhaust aftertreatment system.

Chapter 2: Literature Review

The main goals of this research project were to:

1. Study the effect of hydrocarbon species on NO oxidation over a diesel oxidation catalyst.

2. Spatially resolve the consumption of reactant species in a diesel oxidation catalyst.

This chapter consists of a literature review which provides a background of the previous research that has focussed on NO oxidation, hydrocarbon oxidation, the effect of hydrocarbons on NO oxidation and the spatial resolution of reactant species.

2.1 Overview of the diesel oxidation catalyst

As discussed above, a common catalyst in many current and proposed diesel exhaust gas aftertreatment systems is a diesel oxidation catalyst (DOC). Most DOCs are composed of ceramic cordierite or metal monolith substrates coated with a high surface area alumina- or zeolite-based washcoat. Noble metals, such as Pt, Pd or a Pt/Pd blend, are then dispersed over this washcoat [5]. An example of Pt dispersed over an alumina washcoat is shown in Figure 2-1 [23].
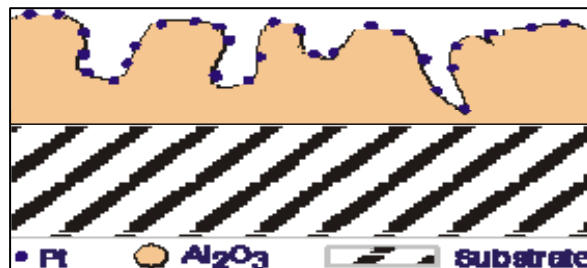
Figure 2-1: Catalyst sites dispersed on a carrier

As compared to Pd, Pt-based DOCs are typically more active for pertinent diesel exhaust oxidation reactions [24]. However, sintering of monometallic Pt DOCs is quicker in an oxygen-rich atmosphere compared to Pt/Pd formulations [25,26], and therefore Pt/Pd catalysts are also studied. Aging of a Pt/γ-Al$_2$O$_3$ DOC with added zeolite for hydrocarbon trapping has been evaluated. The catalyst lost its activity with use. This loss was due to simultaneous thermal and chemical deactivation. The chemical deactivation was caused by lube oil-derived poisons such as P, Zn and Ca along with fuel-derived poisons such as S whose accumulated amounts also increased with mileage [27]. A few ideas have been proposed to explain the higher activity of bimetallic catalysts after thermal ageing. One group has speculated that the reason for the decreased rate of sintering is that at temperatures between 300–700°C the alloy undergoes oxidation to produce less mobile particles on the catalyst surface thus preventing particle growth and maintaining the highly dispersed, large active site surface area [25]. Also, characterization studies of the aged bimetallic Pt/Pd catalyst strongly indicate Pt enrichment within the interiors of the bimetallic core, with Pt surrounded by Pd particles, thus preventing the migration of Pt and maintaining its dispersion even after thermal ageing [28,29]. The maintained precious metal surface area after ageing is the probable cause for the maintained catalytic activity demonstrated by a thermally aged bimetallic DOC for CO and C$_3$H$_6$ oxidation [26]. On a more fundamental level, studies have shown that the aged bimetallic catalyst contains alloyed Pt/Pd particles along with tetragonal PdO particles [26], which are either present at the surface of the bimetallic particles as single crystals or on the oxide support as isolated PdO crystals [25,26].

The importance and current applications of an upstream DOC installed for the performance optimization of downstream after-treatment devices such as NSR, SCR and particulate filters have already been discussed in the introduction. However, DOCs have also been installed by themselves on various engine exhaust trains. DOCs installed on a light duty Hyundai truck helped in the reduction of particulates [30]. Various bus engines equipped with DOCs met smoke and particulate regulations in Europe [31]. A pre-1994 Model Year (MY) 2-stroke bus engine with a DOC resulted in significantly reduced particulate emissions [32]. Reduction in particulate matter emissions over the diesel oxidation catalysts was achieved through the oxidation of the soluble organic fraction (SOF) of the particulate matter which is mainly composed of heavy hydrocarbons. Metallic DOCs coated with upto 30% lower precious metals installed on 2.7L twin turbocharged diesel V-6 European sedan showed equivalent or better performance for lowering hydrocarbon emissions than ceramic ones [33]. This reduction was a result of higher thermal conductivity and lower thermal mass along with the greater mass transfer, mixing and turbulence caused by the shovel structures projecting into the flow channel of the metallic substrate. DOCs installed on medium and heavy duty diesel engines resulted in substantial reduction in particulates, gas phase hydrocarbons and CO [34]. An oxidation catalyst installed on a compressed natural gas (CNG) - fuelled transit bus engine in California resulted in significant reductions in total particulate matter, total hydrocarbons, non methane hydrocarbons and CO [35]. A DOC installed on a 2005 light-duty diesel vehicle resulted in 45 and 43% reductions in CO and hydrocarbon emissions respectively even after aging [36]. A light-duty diesel engine equipped with a DOC comprised of 3:1 Pt: Pd was found to be highly active for CO and total hydrocarbon

reduction. It was also active for NO oxidation which helped reduction of particulate matter through oxidation by NO_2 [37]. Further information concerning DOC technology developments can be found in a review written by Blakeman et al. [38].

2.2 NO oxidation

NO oxidation to NO_2 is important for efficient performance of downstream NO_X storage/reduction (NSR) catalysts, selective catalytic reduction (SCR) catalysts and diesel particulate filters (DPFs). However, NO oxidation to NO_2 is limited by kinetics at low temperatures and by thermodynamics at high temperatures. First, equilibrium between NO and NO_2 is easily achieved over Pt-based catalysts, and its influence is typically observed above 350°C in NO oxidation tests [39]. Mulla and co-authors have studied NO oxidation kinetics over Pt/Al_2O_3 and NSR catalysts and have demonstrated that the rate is ~1st order each in NO and O_2, but has a negative ~1st order dependency in NO_2 [40,41]. This product inhibition imposes significant constraint on conversions. Inhibition of NO oxidation by NO_2 has also been observed over a Pt/SiO_2 catalyst [42]. Segner et al. [43] found that NO_2 easily dissociates into NO and atomic oxygen over the Pt surface due to its strong oxidising ability. Thus, its ability to adsorb preferentially on Pt makes NO_2 a source of surface oxygen. This high coverage of oxygen obtained by exposure to NO_2 was also seen by Parker et al. on a Pt (111) surface [44] and by Zheng and Altman on a Pd (111) surface [45]. The inhibition effect has therefore been attributed to oxygen coverage and the high sticking coefficient of NO_2 on Pt [43,44], preventing other species from gaining access to the surface.

11

Various studies have found that the activity of the catalyst for NO oxidation depends on the size of the Pt particle, where NO oxidation rates are actually improved with larger particle sizes. This observation is true for Pt supported on Al_2O_3 [46-50], SiO_2 [47,48,50] as well as TiO_2 [51] and suggests some amount of thermal aging in practice may actually improve NO oxidation performance. The surface oxygen produced by NO_2 decomposition may interact with the Pt particles to form less active, strong Pt-O bonds [49]. Several studies [52,53,54] have reported that smaller Pt particles require a higher temperature for oxygen desorption than larger particles. Therefore, the Pt-O bonds are weaker and break much easily in case of the large Pt particles [50], making them more active than smaller particles.

2.3 Hydrocarbon oxidation

Diesel exhaust contains many pollutants, including unburned hydrocarbons. There are many studies which have dealt with the oxidation of individual hydrocarbons on noble metals, including kinetic studies in some cases [55,56,57,58]. The oxidation of individual hydrocarbons such as benzene, toluene and xylene have been studied over Pt-Rh [59,60], Pd-Rh [61] and Pt [62,63] catalysts. These studies found that benzene light-off took place before toluene, which was in turn followed by xylene. In terms of mixtures, depending on their relative affinity towards active catalyst sites, different hydrocarbons show different reaction rates [64]. For example, when benzene, toluene, hexene and isooctane are reacted together in the presence or absence of CO, hexene is oxidised first, followed by toluene, benzene and isooctane because the adsorption strength of hexene is higher than the other hydrocarbons and thus adsorbs in preference to

the others in the mixture. This was also reported in previous dynamometer and simulated exhaust studies where the hydrocarbons were removed in the order alkenes → toluene → benzene → alkanes [65,66,67]. Thus, hydrocarbons behave differently when reacted individually and together. Several authors reasoned that this was because the adsorption strength increased with an increase in molecular size [61,68], meaning that benzene was adsorbed weakly and thus was easily oxidised during individual oxidation, compared to toluene and xylene. However, when reacted together, competitive adsorption between the hydrocarbons results in the more strongly adsorbed hydrocarbon being converted first. Because of this difference in the oxidation characteristics of individual and hydrocarbon mixtures, it is important to study and understand the competitive reactions between various hydrocarbons in a mixture.

Other studies have been reported which involve the simultaneous oxidation of mixtures of hydrocarbon compounds such as benzene, toluene, styrene and n-hexane over Pt-based monolithic catalysts [69,70]. Ordonez et al. [69] found that n-hexane did not affect benzene and toluene conversions but the presence of benzene or toluene inhibited n-hexane conversion significantly. Similar results were obtained by Gangwal et al. [71] for mixtures of n-hexane and benzene over a PtNi/γ-Al$_2$O$_3$ catalyst. However, Hermia and Vigneron [72] found that although n-hexane did not affect toluene conversion over a monolithic Pt/Pd catalyst, consistent with the previous studies, but n-hexane conversion shifted to lower temperatures in the presence of toluene, rather than higher. Also, while studying the oxidation of mixtures of n-hexane and toluene over Pt/Al$_2$O$_3$ catalysts with small and large Pt crystallite sizes, Grbic et al. [73] found that the oxidation of each

hydrocarbon was mutually inhibited by the other. Such behaviour was attributed to the competitive adsorption of the hydrocarbons on the same type of active sites. They also found that toluene adsorbed more strongly than n-hexane at larger Pt crystallites and vice versa. Such inhibition was also seen for binary mixtures of benzene and styrene by Barresi and Baldi [70]. The oxidation of benzene and butanol mixtures over Pt/Al$_2$O$_3$ catalysts with varying Pt dispersions was studied by Papaefthimiou et al. [74]. They found that butanol significantly inhibited benzene oxidation. Of interest for DOC application is the study of pertinent competitive oxidation reactions to understand the influence of various species on the reaction rates of the others.

2.4 Effect of hydrocarbons on NO oxidation

Another area that has not gained much attention is the effect of various hydrocarbons on NO oxidation and vice versa. One study [75] has reported that increasing the amount of either CO, NO or propylene lowers the oxidation conversions of both CO and propylene. However, the CO and propylene inhibition effect decreased with temperature while that of NO increased with temperature. Burch and Watling [76] found that the Pt surface is covered by carbonaceous species in presence of alkenes while it is covered by adsorbed oxygen in presence of short-chain alkanes. Because of the low oxygen coverage on the Pt surface in the presence of alkenes, the rate of propylene oxidation has a high order in O$_2$, 1.8, while in presence of alkanes, at lower O$_2$ concentrations the hydrocarbon oxidation rate actually decreases with increasing O$_2$ concentration, eventually remaining unchanged at higher O$_2$ levels, indicating that the Pt surface has a high oxygen coverage which prevents the hydrocarbon from reaching the Pt

surface. Since oxygen is required to produce NO_2 from NO and Pt is relatively oxygen deficient in the presence of propylene, the presence of propylene can hinder NO oxidation due to the absence of surface oxygen, but would favour the reduction of NO to N_2 and N_2O. Another study [77] investigated the effect of hydrocarbons and CO on NO oxidation and NO_2 reduction over a DOC and showed that with aged DOCs, reductants can facilitate the complete reduction of NO_2 to NO. Only once all the reductants were consumed, did the NO oxidize back to NO_2. These findings indicated that for aged DOCs, as long as hydrocarbons and CO are present in the exhaust, NO_2 can be consumed by the DOC, thus hindering the performance of the downstream devices. Similar results have been found in previous studies with Pt/Al_2O_3 catalysts where NO oxidation was inhibited by the presence of CO [75,78,79]. Crocoll et al. [78] found that at temperatures below 250°C, the surface of Pt/Al_2O_3 catalysts was predominantly covered by CO which competed strongly with the oxygen, thus lowering NO oxidation. Over an NSR catalyst also, NO_2 reduction and therefore the observed NO oxidation conversion, is affected by the presence of CO, individually and together with propylene [9]. In this case, CO reduced NO_2 to NO at temperatures >100°C, thus decreasing the amount of NO_X stored on the surface. However, when propylene was present along with CO at low temperature, NO_2 reduction was inhibited, thus improving NO_X storage.

Hammer et al. [80] also observed the influence of hydrocarbons on NO oxidation while studying the effect of adsorption and desorption processes on non-thermal plasma (NTP) enhanced catalytic NO_X reduction over lean NO_X catalysts. They found that in presence of high concentrations of hydrocarbons in diesel exhaust, the oxygen radicals

generated by non-thermal plasma treatment reacted with the hydrocarbons and generated peroxy- radicals. These radicals in turn helped to oxidize NO to NO_2 but did not reduce NO_2 back to NO. Thus, the non-thermal plasma treatment alone (i.e. without the catalyst) can help achieve high NO oxidation conversions even above 300°C (where it is thermodynamically limited in the absence of NTP), as long as the exhaust contains high amounts of hydrocarbons.

2.5 Spatial resolution of reactant species consumption

A technique known as spatially resolved capillary-inlet mass spectrometry (SpaciMS) was developed to spatially resolve reaction chemistry within monolith-supported catalysts [81,82]. This technique involves the use of capillary tubes inserted within the channels of the monolithic catalyst. The outlets of these capillaries are connected to a mass spectrometer which enables measurements of the concentrations of the various species at various locations within the monolith, and therefore a detailed picture of the spatio-temporal patterns of reaction fronts can be obtained.

This technique was used to study the evolution of various species within the channels of a monolithic $Pt/K/Al_2O_3$ NSR catalyst in order to understand the chemistry and sequence of reactions occurring during the regeneration phase [83,84]. As an example of their findings, they showed that during the NSR regeneration phase, the oxidation of CO, with complete consumption of O_2, occurred at the catalyst front [84]. The resulting exotherm spread slowly downstream over time, raising the temperature for subsequent NO_X storage significantly. H_2 appeared, from the water-gas-shift reaction,

only at those positions and times when almost all the O_2 was consumed and NO_X release/reduction was nearly complete, i.e. when CO consumption via other reactions ended.

The effects of sulphur on the spatio-temporal distribution of reactions within a commercial, monolithic NSR catalyst was also studied using the SpaciMS technique [85,86]. The authors demonstrated that prior to sulphur exposure, high NO_X conversions were achieved at high temperatures (100% at 325 and 400°C) as well as at lower temperatures (96% at 200°C). These high conversions were attained with just the front half of the catalyst at high temperatures while lower temperatures required nearly the entire catalyst length [86]. The area over which the NSR reactions occurred was labelled the NSR zone. The rest of the catalyst was also active for O_2 storage/reduction (OSR zone). Upon sulphur exposure, the sulphur accumulated in a plug-like manner, which began at the catalyst inlet and then slowly moved downstream [85]. The accumulation of sulphur moved the NSR zone downstream and shortened the OSR zone. With S exposure, NO_X storage sites were poisoned to a greater extent than oxygen storage sites [86], lowering the catalyst activity for NSR reactions in the sulphur-poisoned area, although some OSR and NO oxidation activity were retained [85].

SpaciMS has also been used to measure the concentrations of transient species as well as resolve the distribution of their concentrations across and within fuel cells [87]. Measurements of transient phase hydrogen, oxygen, water and dilute concentration dynamics related to load switching indicate that the reaction chemistry under their test

conditions was limited by oxygen. Moreover, intra-fuel cell oxygen concentration measurements helped understand its distribution at various loads and thus, identify intra-cell concentration gradients, non-uniformities as well as anomalous operation.

Chapter 3: Experimental Work

A monolith-supported Pt-Pd/Al$_2$O$_3$ sample with 8 g/ft^3 loading of 1:2 Pt:Pd, was used in these experiments. The low precious metal loading was used so that differential region operation, where changes in gas concentrations are clearly visible, could at times be evaluated. This is an important consideration when finding data for model input, which was also an objective of these experiments (in terms of the collaboration with GM). The sample was 35 mm in length and 20.4 mm in diameter and was inserted into a horizontal quartz tube reactor which was placed inside a temperature-controlled furnace (manufactured by Lndberg/Blue), as shown in Figure 3-1. The catalyst was wrapped with high-temperature 3M matting material to cover the gap between the catalyst and the reactor wall to ensure that no gas slipped around the sample. Two K-type thermocouples were placed within one of the radially centered channels; one just inside the inlet face of the catalyst and one just inside the outlet face of the catalyst. Another thermocouple was placed ~2" upstream of the sample.
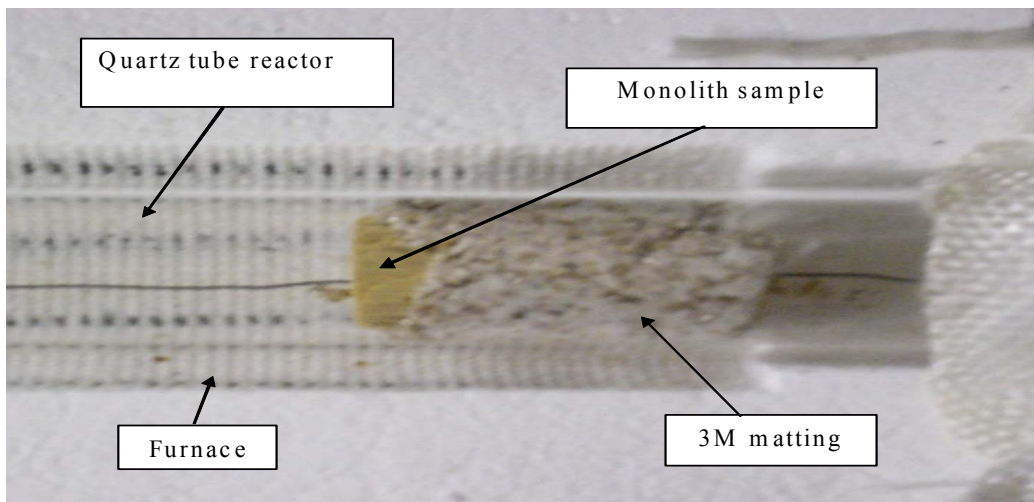
Figure 3-1: Schematic of monolith inside the quartz tube reactor

In comparing experiments with and without CO_2, no influence on the oxidation reaction rates was observed and since the presence of CO_2 makes CO oxidation difficult to clearly observe using our instrumentation, CO_2 was not added to the experiments described below. Gases and gas mixtures were supplied by Praxair and were metered via calibrated Bronkhorst mass flow controllers. The mixture of gases excluding carbon-containing molecules was sent through a high-capacity furnace (preheater) manufactured by Watlow, achieving the target test temperature prior to entering the tube furnace holding the sample, as shown in Figure 3-2. This minimized any artificial axial and radial temperature gradients during experiments. Dodecane and/or m-xylene (laboratory grade supplied by Fisher Scientific) were injected directly into the quartz tube reactor using a syringe pump and part of the total N_2 flow as the carrier gas. When CO and propylene were used, they were also introduced with the N_2 carrier for the dodecane. This avoided any reactions between the carbon-containing species and O_2 on the hot upstream steel tubing. Dodecane injection began at an average catalyst temperature of about 120°C (average of temperatures measured by the inlet and outlet thermocouples shown in Figure 3-2). The gases exiting the reactor were maintained at >120°C to avoid condensation.
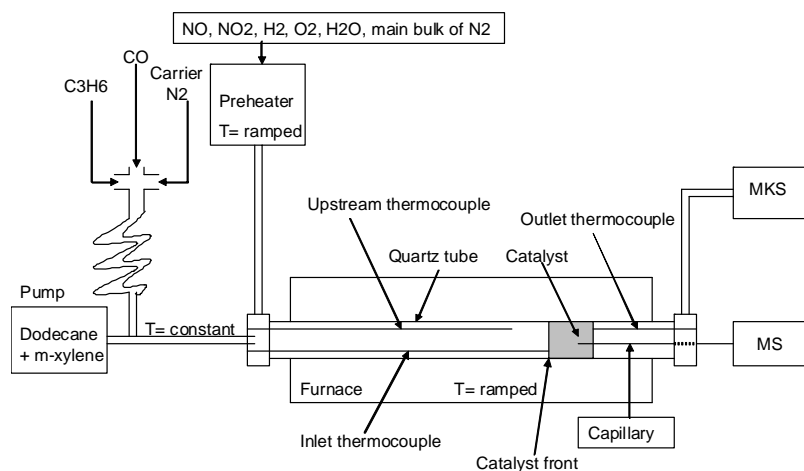
Figure 3-2: Schematic of gas delivery and gas analysis set up

3.1 Experiment Types

3.1.1 Effect of hydrocarbon species on NO oxidation over diesel oxidation catalysts

In this set of experiments, the effect of various hydrocarbon species, and their concentrations, as a function of temperature on NO oxidation was evaluated through temperature programmed oxidation experiments. The feed stream during the experiments contained different concentrations of gases including NO, NO_2, C_3H_6, C_8H_{10} and $C_{12}H_{26}$. Oxygen and H_2O were included in all experiments, and N_2 was used as the balance gas. The gas flow rate used was 19.06 L/min (equivalent to a space velocity of 100,000 hr^{-1}). During each experiment, the catalyst temperature was ramped at approximately 7.5°C/min. Initially, tests with no reactant gases were performed and there was a maximum of 4°C difference between the front and back of the sample during these "blank" temperature ramps.

The exiting gas compositions were measured using a MKS MultiGas 2030 FTIR analyzer at approximately a 2 Hz collection rate. CO, CO_2, NO, NO_2, N_2O, NH_3, C_3H_6, C_8H_{10}, $C_{12}H_{26}$ and H_2O concentrations were measured.

The temperature ramps for experiments that included $C_{12}H_{26}$ were stopped at temperatures just above 300°C. This was due to $C_{12}H_{26}$ cracking upstream of the catalyst as measured by a mass spectrometer and hence the results for the temperature ramps are shown only to these temperatures.

3.1.2 Spatial resolution of reactant species consumption in diesel oxidation catalysts

The aim of this set of experiments was to spatially resolve various reactant species along the length of the catalyst i.e. in the axial direction only, under constant ("steady-state experiments") and varying ("temperature ramps") temperature conditions. The feed stream during the experiments contained 425 ppm $C_{12}H_{26}$, 800 ppm C_3H_6, 800 ppm CO, 100 ppm NO, 160 ppm H_2, 10% O_2, 5% H_2O, 1.3% He and a balance of N_2. This composition was suggested by GM (in terms of the collaboration). The spatial resolution was achieved by placing a silica capillary within one of the radially centered catalyst channels. The capillary dimensions were 0.3 mm I.D. and 0.43 mm O.D. The end of this silica capillary was connected to the sampling end of a 6' capillary from a Hiden Analytical mass spectrometer via a zero dead volume steel union fitting. Samples were collected at different positions by moving the silica capillary tip to different positions within the channel, as shown in Figure 3-3. Outside of the reactor, both the capillaries were heated and insulated along their entire lengths to avoid water condensation. Note that Figure 3-3 is only used to illustrate the different capillary positions. For these experiments, only one capillary was inserted within one channel of the monolith to study the axial (not radial) distribution of the species.
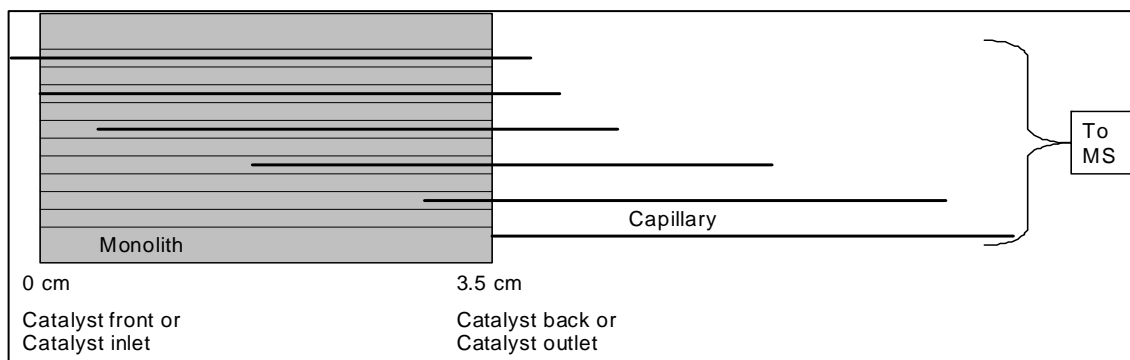
Figure 3-3: Capillary setup within the monolith

The gases measured by the mass spectrometer were H_2, H_2O, NO, NO_2, O_2, C_3H_6, CO_2, He and $C_{12}H_{26}$. He was added to the reaction mixture to act as a tracer in the mass spectrometer and was used for calibration purposes as described later. The MKS 2030 FTIR was also used to measure species concentrations at the reactor outlet and to verify calibration accuracy.

In the "steady state" experiments, the upstream temperature was kept constant and the capillary was pulled to different positions along the catalyst length. This was then repeated at a different temperature. The gas flow rate used was 19.06 L/min (equivalent to a space velocity of 100,000 hr^{-1}).

In the "temperature ramp" experiments, the temperature was ramped with the capillary at a fixed position within the channel. This was then repeated with the capillary pulled to another position. The gas flow rates used were 19.06 L/min (space velocity = 100,000 hr^-1) and 10 L/min (space velocity = 52,500 hr^{-1}). The ramping rate for the high

flow rate experiments was ~7.5°C/min while that for the low gas flow rate was ~8.1°C/min.

In order to more clearly present the data and compare the results of the temperature ramp experiments, the temperature data for each experiment were first lined up with respect to time, so that the start time of each temperature ramp matched. These offset times were used for the final plot of temperature and concentration or conversion versus time. This technique was possible because the temperature ramps were consistent in every experiment as measured by the thermocouple placed ~2" upstream of the catalyst. Furthermore, prior to testing, several "blank" experiments were run with no reactants and the temperature ramp data as measured at the catalyst inlet and outlet faces were similar (< 4°C difference).

To calibrate the data obtained by the MS, the partial pressures of the species were first divided by the measured partial pressure of He and then multiplied by the percentage of He used in the experiment. The initial and final partial pressures for each gas were calibrated to concentration using corresponding concentrations measured by the MKS. The calibration was then applied to the ratio of the partial pressures of the gas species to He, resulting in the given concentrations. A detailed explanation of the calibration procedure is given in Appendix A.

Chapter 4: Effect of hydrocarbon species on NO oxidation over diesel oxidation catalysts - Results and Discussion

In this section, temperature programmed oxidation experiments were performed to understand the effect of various hydrocarbon species, and their concentrations on NO oxidation. During each experiment, the temperature was ramped at ~7.5°C/min.

First, a baseline NO oxidation experiment was performed and the data are shown in Figure 4-1. During this experiment, the feed stream contained 200 ppm NO, 10% O_2, 5% H_2O and a N_2 balance. Oxidation conversion was measurable at 140°C, reached a maximum of about 33% at 420°C and then decreased. As mentioned, this trend is due to NO oxidation being kinetically limited at lower temperatures and thermodynamically limited at higher temperatures [39]. NO_2 product inhibition contributes to the low conversions observed until thermodynamic limitations are reached [40,41]. The data obtained from experiments containing C_3H_6 in the mixture are also presented in Figure 4-1. In performing these experiments, the temperature ramp was ended at approximately 470°C. With C_3H_6 in the feed, the maximum conversions were measured at this maximum temperature, suggesting higher conversions might have been attained if the temperature ramp was continued to higher temperatures. The data clearly show that the addition of C_3H_6 resulted in a significant decrease in NO conversion to NO_2. With the smallest addition shown in this figure, 100 ppm, NO oxidation was not measured until 210°C, and the maximum conversion was 20% at 470°C. Increasing the C_3H_6 concentration from 100 to 1000 ppm led to further drops in NO conversion, reaching only

7% at 460°C with 1000 ppm added. These data clearly demonstrate that C_3H_6 results in lower NO_2 produced and that as the C_3H_6 concentration was increased from 100 to 1000 ppm, NO oxidation was further hindered.
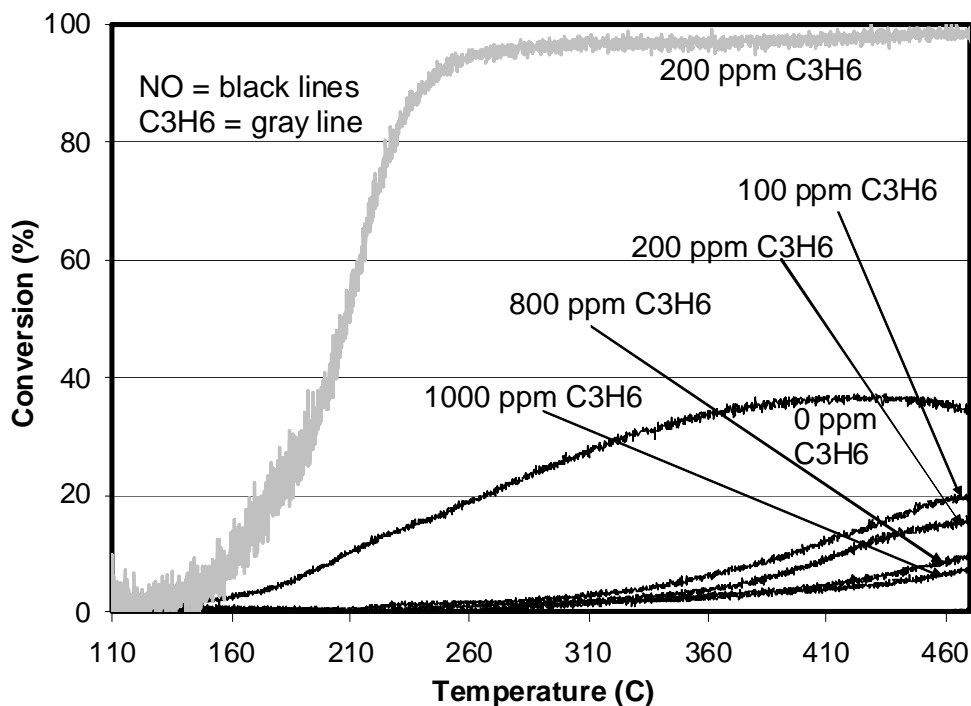
Figure 4-1: NO and C_3H_6 oxidation conversion as a function of temperature and C_3H_6 concentration. The feed stream contained 200 ppm NO, 10% O_2, 5% H_2O and either 0, 100, 200, 800 or 1000 ppm C_3H_6, and a balance of N_2.

There are several possibilities that could explain this effect. Simple competition for O_2 is unlikely since O_2 is present in large excess even at the highest C_3H_6 concentrations. For example, the complete oxidation of 1000 ppm propylene requires an oxygen concentration of 0.45%, which would leave 9.55% oxygen in the stream. Although, carbonaceous species derived from alkenes are known to poison Pt sites [76], it is not likely solely due to such poisoning, since C_3H_6 oxidation begins at 150°C (example data are shown in Figure 4-1) and is almost completely converted above 260°C,

where the measured NO_2-out levels are still far smaller than those with no C_3H_6. The likely reason for the observed results is that the NO_2 formed is being consumed as an oxidant in the C_3H_6 oxidation reaction, resulting in the overall appearance of NO oxidation inhibition. This mechanism follows that described in an earlier study, which showed that in the presence of CO and hydrocarbons, an aged DOC will reduce any NO_2 produced from NO oxidation, until all reductants are consumed [77].

Experiments were run with NO_2 as the inlet NO_X source instead of NO in order to further study this phenomenon. Data obtained from a baseline NO_2 reduction experiment are shown in Figure 4-2. The NO_2 concentration began decreasing at about 300°C, which is a result of thermodynamic equilibrium between NO and NO_2 being attained over the catalyst. This is similar to the results obtained by Olsson et al. [39] where thermodynamic equilibrium between NO and NO_2 over Pt/Al_2O_3 catalysts was readily achieved at temperatures > 350°C. Also shown in Figure 4-2 is the effect of different hydrocarbons on NO_2 reduction, or what can also be considered as the use of NO_2 as the hydrocarbon oxidant. Because the three different hydrocarbons have different C-to-N ratios, the experiments were conducted with different concentrations resulting in each experiment having a comparable C:N ratio. The addition of any of the three hydrocarbons used caused NO_2 reduction to occur at significantly lower temperatures than that seen in their absence. In the presence of hydrocarbon, the primary product observed was NO. Some N_2O was also observed after hydrocarbon oxidation and NO_2 reduction began, but dropped off as the hydrocarbons neared complete oxidation. An example of the N_2O formed during the m-xylene-containing experiment is plotted. We can see that the N_2O

formation began around 235°C, after the start of hydrocarbon oxidation and NO_2 reduction, and was absent by about 385°C, where the hydrocarbons were almost completely oxidised. Also, the formation of a small amount of N_2 via hydrocarbon SCR completes the mass balance on NO_X. Again for example, with m-xylene added, and at ~284°C, the measured concentration of outlet NO and N_2O is ~159 and 11 ppm respectively, while the inlet NO_2 was 202 ppm. Therefore, in order to close the mass balance, the concentration of N_2 must be approximately 10.5 ppm. Although equivalent C:N ratios were used, NO_2 reduction by C_3H_6 started at a lower temperature than that observed with $C_{12}H_{26}$ and m-xylene, whereas with these two larger molecules similar results were obtained. This demonstrates that the NO_2 reduction by the hydrocarbon, or NO_2 oxidation of the hydrocarbon, is dependent on the type of hydrocarbon itself.
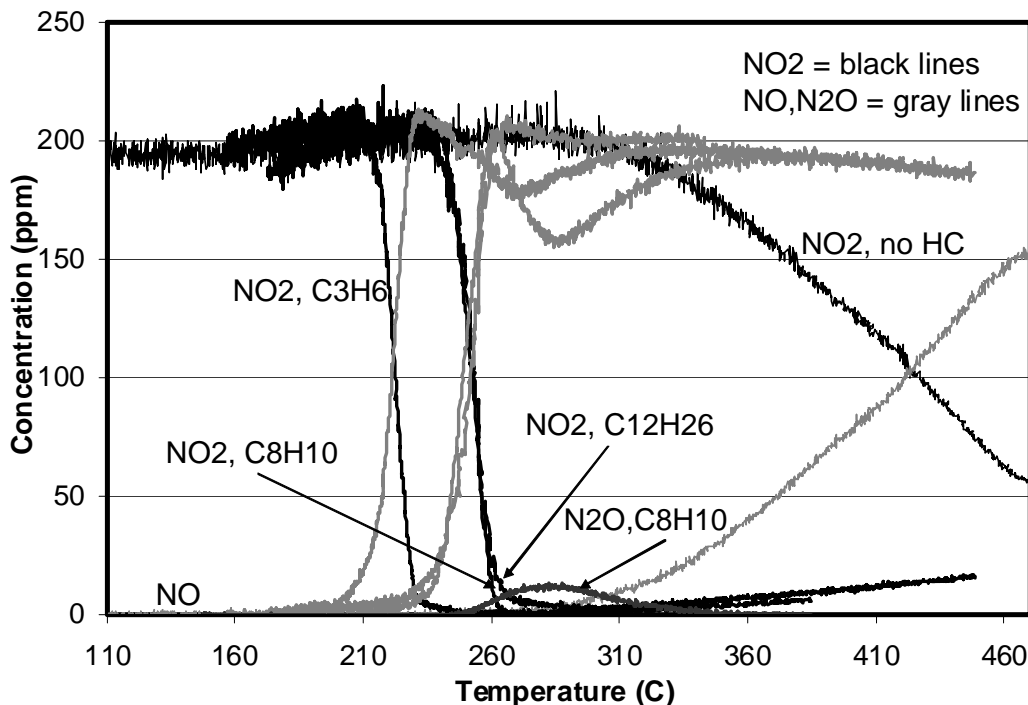
Figure 4-2: NO_2 reduction as a function of temperature and hydrocarbon type. The feed stream contained 200 ppm NO_2, 10% O_2, 5% H_2O and either no HC or 800 ppm C_3H_6, 300 ppm C_8H_{10} or 200 ppm $C_{12}H_{26}$, and a balance of N_2.

Different C_3H_6 levels were used to investigate the impact of hydrocarbon concentration on NO_2 reduction, with the data shown in Figure 4-3. With every increase in propylene concentration, reduction began at lower temperature. For example the temperature where C_3H_6 oxidation began shifted from 190 to 160°C for 40 and 150 ppm, respectively. The extent of NO_2 reduction was increased as well, with the minimum NO_2 dropping from 25 to 10 ppm. Furthermore, as more C_3H_6 was added, the temperature range across which reduction occurred became smaller. Both the smaller amount of NO_2 and the more rapid reduction as a function of temperature make sense as there is more reactant available for the reaction. These data show that the temperature where hydrocarbon oxidation via NO_2 begins is not only dependent on the hydrocarbon species (Figure 4-2), but also on the amount of hydrocarbon present.
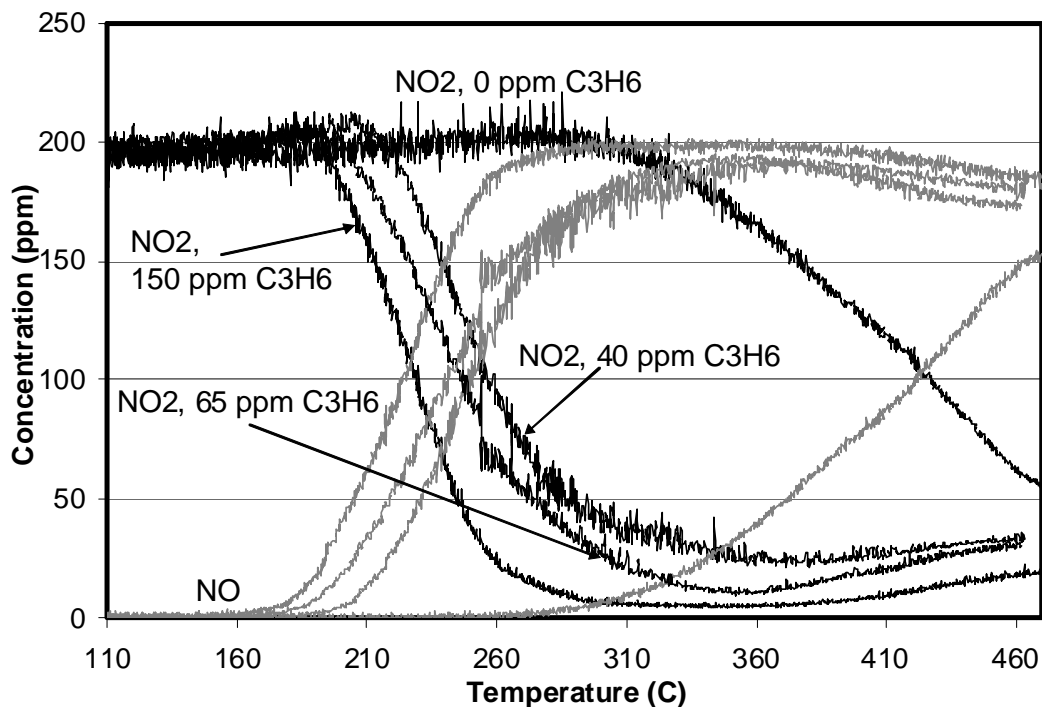

Figure 4-3: NO_2 reduction as a function of temperature and C_3H_6 concentration. The feed stream contained 200 ppm NO_2, 10% O_2, 5% H_2O and either 0, 40, 65 or 150 ppm C_3H_6, and a balance of N_2.

The efficiency of NO_2 as the oxidant relative to O_2 was evaluated by studying the effect of different O_2 concentrations on NO_2 reduction and C_3H_6 oxidation. The NO_X data are plotted in Figure 4-4. There was no significant change in the observed onset temperature for NO_2 reduction for the two cases with low O_2 (0.02 and 0.075% O_2), suggesting that O_2 does not influence NO_2's participation in C_3H_6 oxidation. However, the test with higher O_2 concentration showed a lack of complete NO_2 reduction at the higher temperature, as well as a slightly slower drop in NO_2 as the temperature decreased, likely related to some NO oxidation beginning as well as the presence of large amounts of O_2 inhibiting the reduction via a shift in the equilibrium. Previous work has shown that with Pt/Al_2O_3 catalysts, a greater oxygen surface coverage exists in the presence of high O_2 concentrations, as well as in the presence of NO_2 since NO_2 is a strong oxidizer [39]. The onset of NO_2 reduction in presence of 10% O_2 occurs at a slightly lower temperature and is related to C_3H_6 oxidation beginning at a lower temperature as will be discussed below.

Almost all of the NO_2 is consumed in all the test runs (Figure 4-4), while with the high O_2 level runs, the O_2 is obviously not. This indicates that the NO_2 is being consumed preferentially relative to the O_2. For example, if NO_2 and O_2 were equal as oxidants, both would be consumed equally. The hydrocarbon balance, however, dictates that the O_2 is not being completely consumed. For 150 ppm C_3H_6 entering, only 675 ppm of O_2 would be required to consume all the C_3H_6. With 10% O_2 entering, this would mean less than 1% of the O_2 could be consumed, while still with 10% O_2 in the feed, more than 95% of the NO_2 is consumed, clearly demonstrating preferential use of the NO_2.
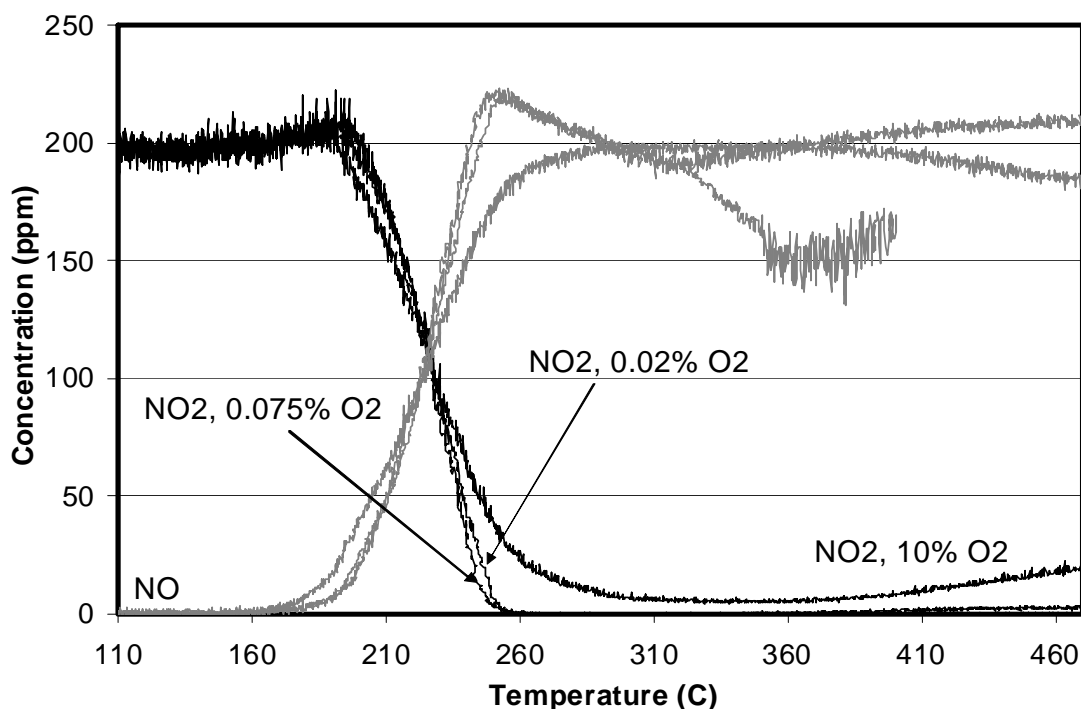
Figure 4-4: NO_2 reduction as a function of temperature and O_2 concentration. The feed stream contained 200 ppm NO_2, 5% H_2O, 150 ppm C_3H_6, and either 0.02, 0.075 or 10% O_2 and a balance of N_2.

The effect of varying the amount of O_2 on C_3H_6 oxidation is shown in Figure 4-5. Two data sets plotted were run without NO_2 or NO in the feed stream. With the lower O_2 concentration (0.075% O_2), there is 10% O_2 excess to facilitate complete C_3H_6 combustion. For the NO_X-free experiments, C_3H_6 light-off occurred at approximately the same temperature for the two O_2 levels tested. In the case with 10% oxygen, however, the decrease in C_3H_6 concentration was steeper and therefore occurred within a narrower temperature window, between about 185–250°C. This is due to the significant excess O_2 in the feed. Also, complete combustion of C_3H_6 is observed with the lower O_2 experiment, but not with the higher. This could be due to the large amount of O_2 resulting in active site saturation, preventing the remaining C_3H_6 from reaching the surface, similar to the argument described above concerning the lack of complete NO_2 reduction.

Figure 4-5: C_3H_6 oxidation as a function of temperature, O_2 concentration and NO or NO_2 presence. The feed stream contained 5% H_2O, 150 ppm C_3H_6, with either 0.075 or 10% O_2, either 0 or 200 ppm NO_2 or NO and a balance of N_2.

Also shown in Figure 4-5 is the effect of adding NO_2 or NO on C_3H_6 oxidation. C_3H_6 oxidation light-off occurred at the same temperature when NO_2 was or was not included with either 0.075% or 10% oxygen. The data shown in Figure 4-4 indicated O_2 had little to no effect on NO_2 reduction via C_3H_6 oxidation while the data in Figure 4-2 indicated that the use of NO_2 as an oxidant depended on the hydrocarbon species. Also, the data in Figure 4-3 showed that the onset of C_3H_6 oxidation varied with C_3H_6 level. Combined, these data indicate that the low temperature reaction constraint or onset of the reaction is activation of the C_3H_6 or hydrocarbon molecule. Once the hydrocarbon is activated, the NO_2 is preferentially consumed as an oxidant. The addition of NO_2 to 0.075% O_2 initially appears to slightly accelerate the C_3H_6 oxidation reaction, relative to

no NO$_2$, but then inhibits it after light-off has occurred. This is especially evident in the 240 to 260°C temperature range as highlighted in Figure 4-6. This is not due to a switch between NO$_2$ and O$_2$ as oxidants, as the conversion is actually worse after 250°C relative to the data obtained in the absence of NO$_2$.
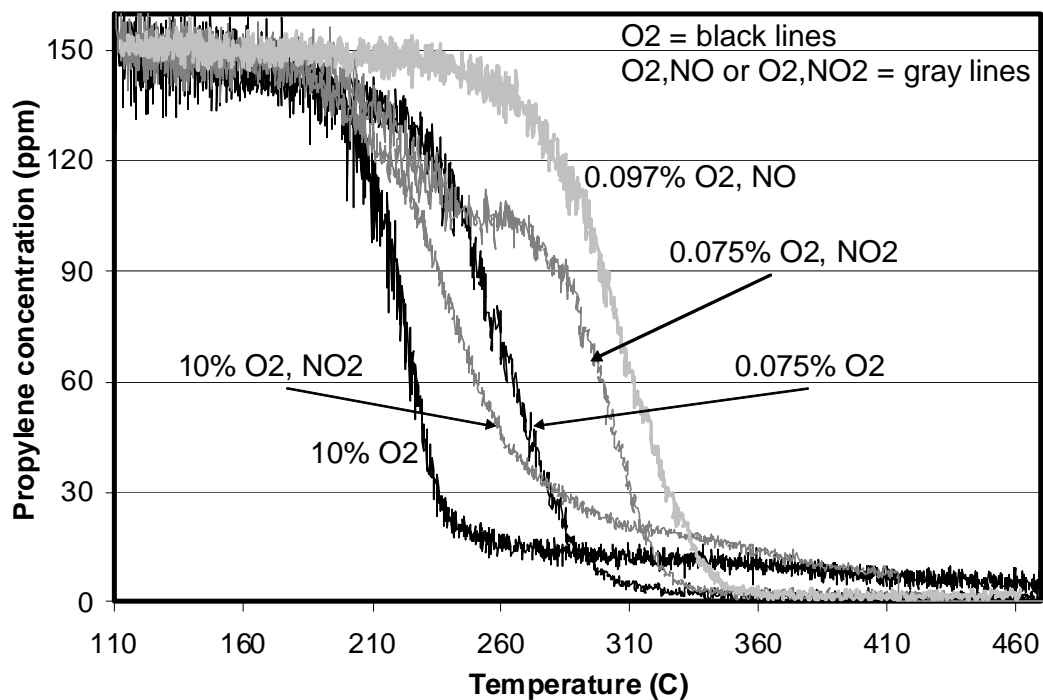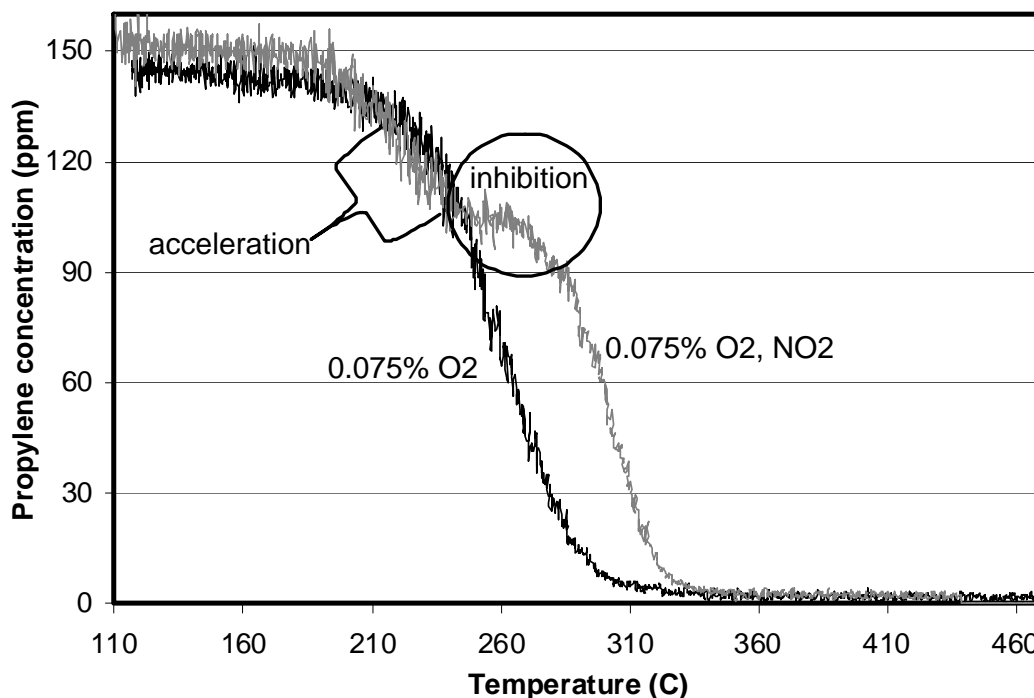

Figure 4-6: C$_3$H$_6$ oxidation as a function of temperature, O$_2$ concentration and NO$_2$ presence. The feed stream contained 5% H$_2$O, 150 ppm C$_3$H$_6$, 0.075% O$_2$, either 0 or 200 ppm NO$_2$ and a balance of N$_2$.

In the experiment with the higher O$_2$ level, this apparent NO$_2$ inhibition effect is seen throughout the experiment (Figure 4-5). This negative effect is attributed to NO inhibition of the C$_3$H$_6$ oxidation reaction, with the NO formed from NO$_2$ reduction. As confirmation, the data obtained from an experiment with NO in the feed are also shown in Figure 4-5. In this experiment, a slightly larger excess of O$_2$ was added to compensate for the O species lost with the removal of NO$_2$. The addition of NO caused C$_3$H$_6$

oxidation light-off to occur at a higher temperature, resulting in less C_3H_6 conversion below 330°C, in comparison to experiments not containing NO_X.

For the experiments containing NO_2 and low-O_2, this is highlighted in Figure 4-7. NO_2 reduction and C_3H_6 oxidation are clearly accompanied by the production of NO and the inflection in the C_3H_6 concentration profile is observed in the same temperature range where NO is produced. This inflection is more pronounced in the region where maximum NO is observed. Although N_2O was also produced in that same temperature range, it was only seen in the experiments containing 150 ppm C_3H_6 and lower O_2 concentrations and was not observed in the data set obtained with 150 ppm C_3H_6 and 10% O_2 and therefore is not considered as the inhibiting factor.
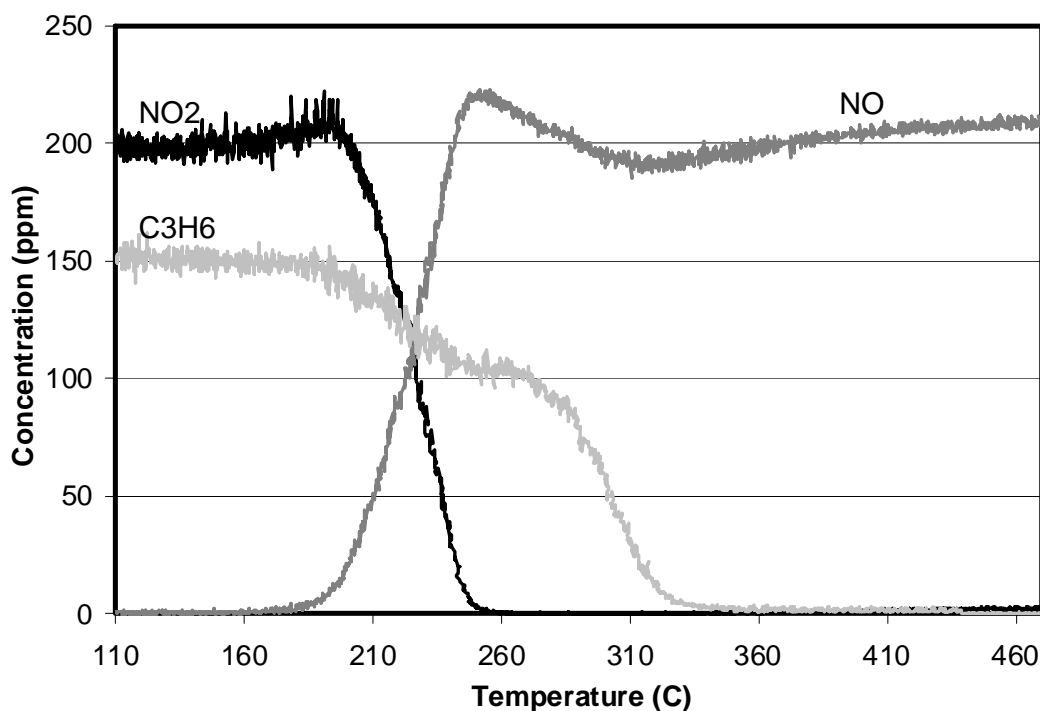
Figure 4-7: C_3H_6, NO and NO_2 concentrations as a function of temperature. The feed stream contained 5% H_2O, 150 ppm C_3H_6, 0.075% O_2, 200 ppm NO_2 and a balance of N_2.

To further evaluate the inhibition of C_3H_6 oxidation by NO, experiments were conducted with varying NO concentrations, with the results presented in Figure 4-8. C_3H_6 light-off shifts to higher temperatures with increasing amounts of NO, confirming that NO inhibits C_3H_6 oxidation. Such an inhibition effect was also seen by Voltz et al. over Pt-containing catalysts [75]. Active site saturation by NO may be preventing C_3H_6 from reaching the surface, thus inhibiting propylene oxidation.
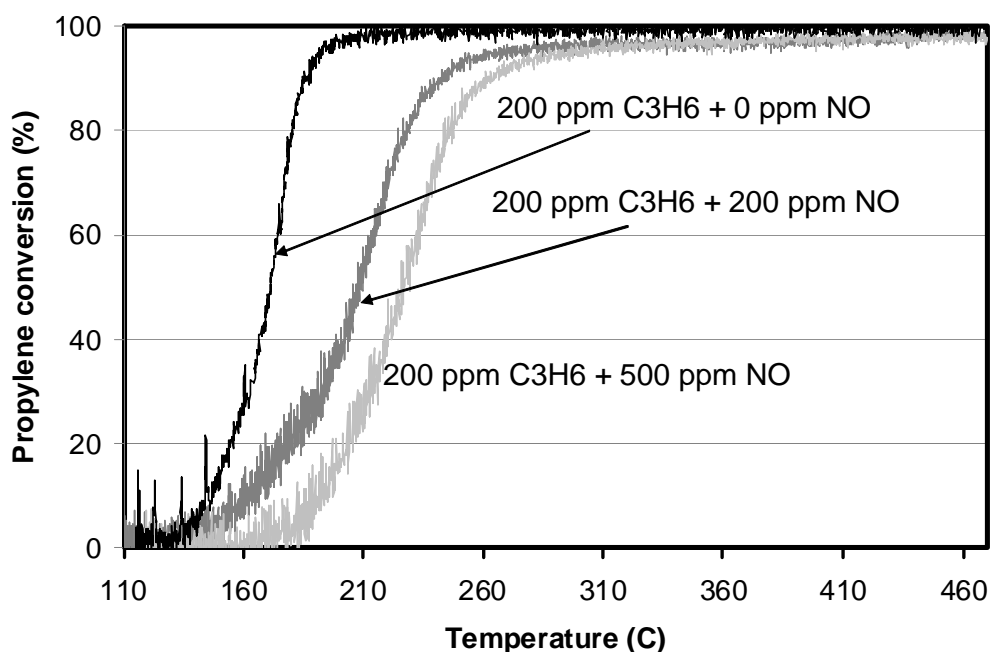
Figure 4-8: C_3H_6 oxidation conversion as a function of temperature and NO concentration. The feed stream contained 5% H_2O, 200 ppm C_3H_6, 10% O_2, with either 0, 200 or 500 ppm NO and a balance of N_2.

In conclusion, hydrocarbons affect NO oxidation over a Pt-Pd/Al_2O_3 catalyst. Increasing amounts of C_3H_6 resulted in lower NO conversion which was due to the consumption of product NO_2 as an oxidant in C_3H_6 oxidation. This was verified by studying the effect of increasing C_3H_6 concentrations and different hydrocarbon species

on NO_2 reduction. The addition of hydrocarbons decreased the NO_2 reduction temperature, as did increasing amounts of hydrocarbons. Inversely, the presence of NO_2 initially accelerated C_3H_6 oxidation but inhibited it at higher temperatures due to the formation of NO, which was shown to inhibit C_3H_6 oxidation.

Chapter 5: Spatial resolution of reactant species consumption in diesel oxidation catalysts – Results and Discussion

5.1 Steady-state experiments

In these experiments, a fixed inlet temperature was established and then the gas species concentrations as a function of catalyst length (i.e. in the axial direction only) were measured over the same monolithic diesel oxidation catalyst as that used for the study in Chapter 4. The feed stream contained 425 ppm $C_{12}H_{26}$, 800 ppm C_3H_6, 800 ppm CO, 100 ppm NO, 160 ppm H_2, 10% O_2, 5% H_2O, 1.3% He and a balance of N_2. The concentrations of NO_2, $C_{12}H_{26}$, C_3H_6, H_2, and CO_2 are plotted, with H_2O, O_2, and NO also tracked. In the data below, NO_2 is plotted instead of NO because NO_2 reduces back to NO within the mass spectrometer, thus the NO concentration would appear unchanged. However, this is accounted for via the NO_2 signal calibration and hence does not affect the results shown. Also, the CO_2 concentration is divided by 5 in the data shown below (Figures 5-1 to 5-5).

The first experiment was carried out at an upstream temperature of 128°C, with data shown in Figure 5-1. There was no change in the concentrations of the various species indicating that there were no oxidation reactions occurring through the catalyst at this temperature. A negligible temperature difference was observed across the catalyst length.
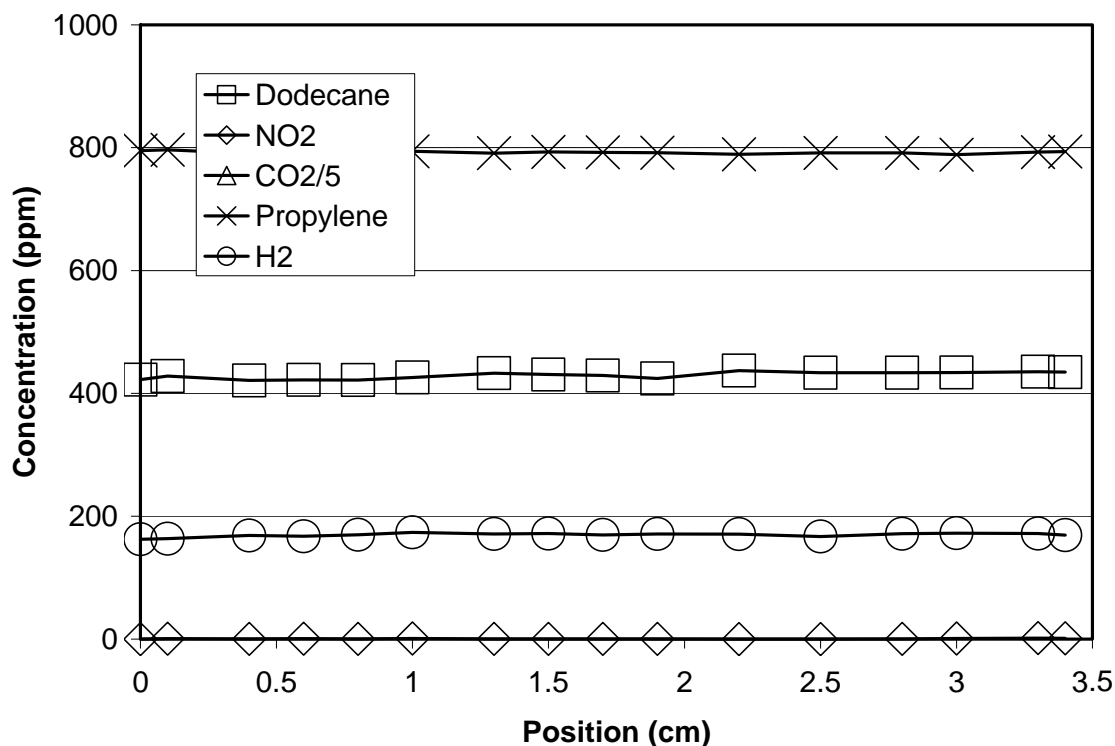
<u>Figure 5-1</u>: $C_{12}H_{26}$, NO_2, CO_2, C_3H_6 and H_2 concentrations as a function of position (distance from the inlet) within the catalyst at an upstream temperature of 128°C.

The next experiment was carried out at 168°C and the data are presented in Figure 5-2. The concentration of H_2 decreased slightly while that of CO_2 increased proportionally. The changes in both occurred at the same positions, between 1 and 2.5 cm from the inlet. The concentration of the hydrocarbon species remained unchanged indicating that there was no oxidation of these species at this temperature. A maximum NO_2 concentration of about 4 ppm was produced at this temperature. The difference in temperature across the catalyst, in the axial direction was approximately 5°C. This is due to the small amount of heat generated by the oxidation of H_2 and CO at this temperature.
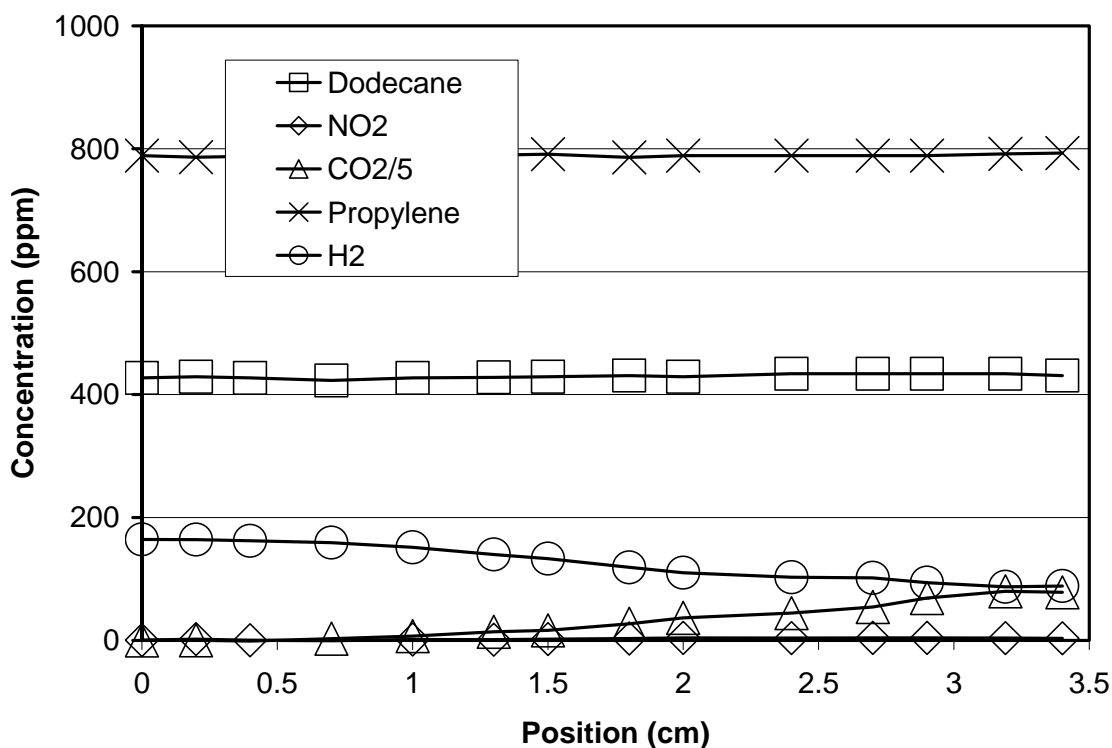
Figure 5-2: $C_{12}H_{26}$, NO_2, CO_2, C_3H_6 and H_2 concentrations as a function of position within the catalyst at an upstream temperature of 168°C.

A similar trend was observed at 208°C, as shown in Figure 5-3, but with the change in CO_2 and H_2 concentration taking place along most of the catalyst length. The hydrocarbon concentrations still remained unchanged, while about 10 ppm NO_2 was observed. The temperature difference across the catalyst length i.e. in the axial direction, after steady state was reached was about 15°C, higher than that observed with the 168°C inlet temperature test because more H_2 and CO was oxidized thereby releasing more heat.
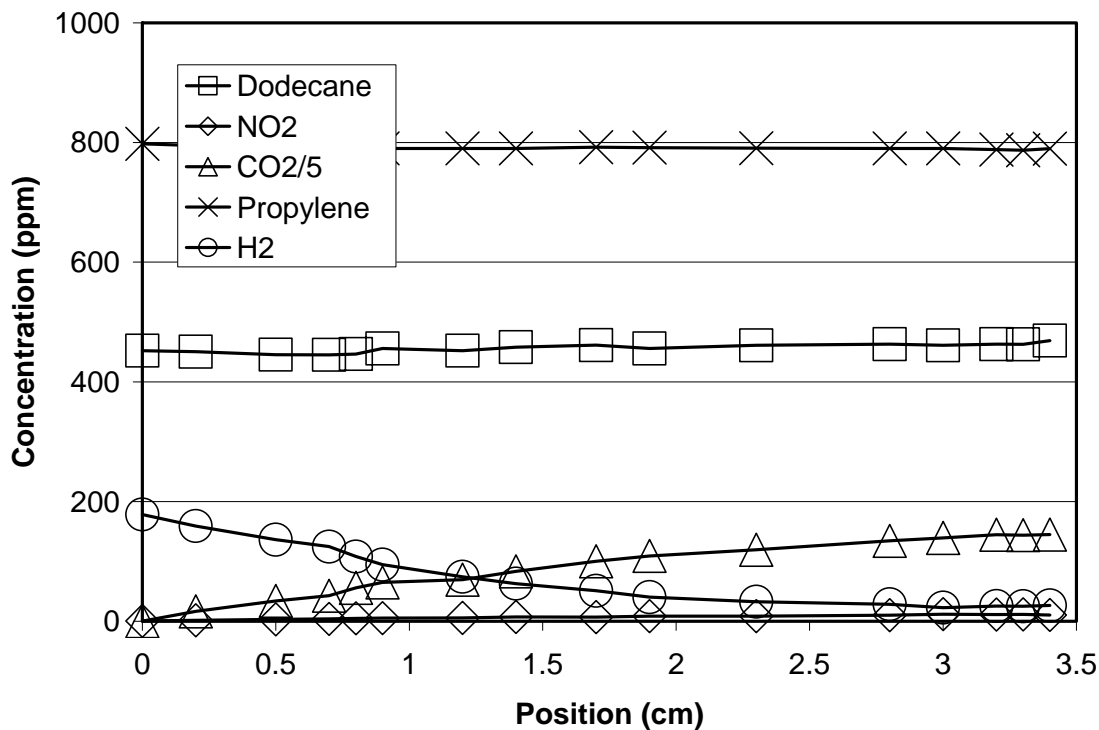
Figure 5-3: $C_{12}H_{26}$, NO_2, CO_2, C_3H_6 and H_2 concentrations as a function of position within the catalyst at an upstream temperature of 208°C.

Increasing the temperature to 248°C (Figure 5-4) resulted in CO and H_2 oxidation shifting further upstream, taking place between the inlet face and 2 cm into the catalyst. Changes in the dodecane and propylene concentrations are observed as well, occurring between 0.7 and 2.3 cm within the catalyst. Significant NO oxidation, which is marked by a significant increase in NO_2 concentration, took place between 0.7 and 2.3 cm inside the catalyst. The maximum NO_2 concentration obtained was about 74 ppm. The temperature difference across the catalyst length was ~120°C, with hydrocarbon oxidation now also contributing to the amount of heat generated.
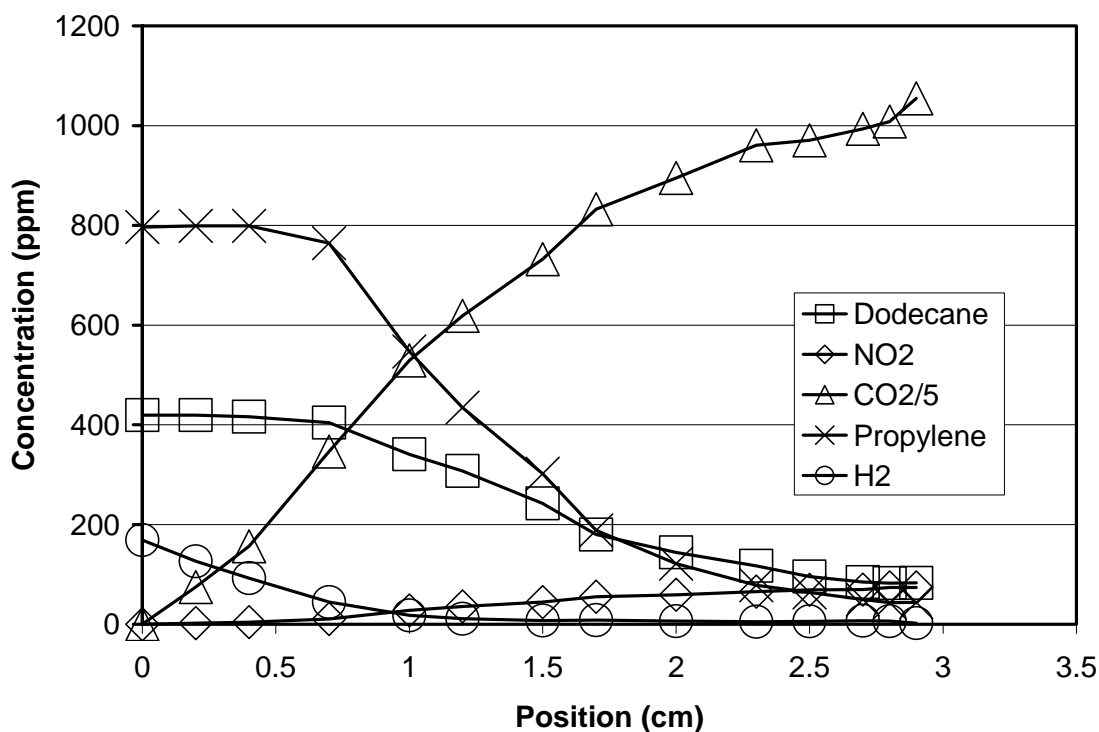
Figure 5-4: $C_{12}H_{26}$, NO_2, CO_2, C_3H_6 and H_2 concentrations as a function of position within the catalyst at an upstream temperature of 248°C.

The data shown in Figure 5-5 were obtained at an inlet temperature of 290°C. H_2 oxidation occurred between 0 and 1.4 cm. The dodecane and propylene concentrations decreased between the inlet face and 1.9 cm into the catalyst. The NO oxidation also shifted closer to the catalyst inlet, taking place between the inlet and 1.9 cm, with a maximum NO_2 concentration of 80 ppm. The temperature difference across the catalyst length was ~140°C.
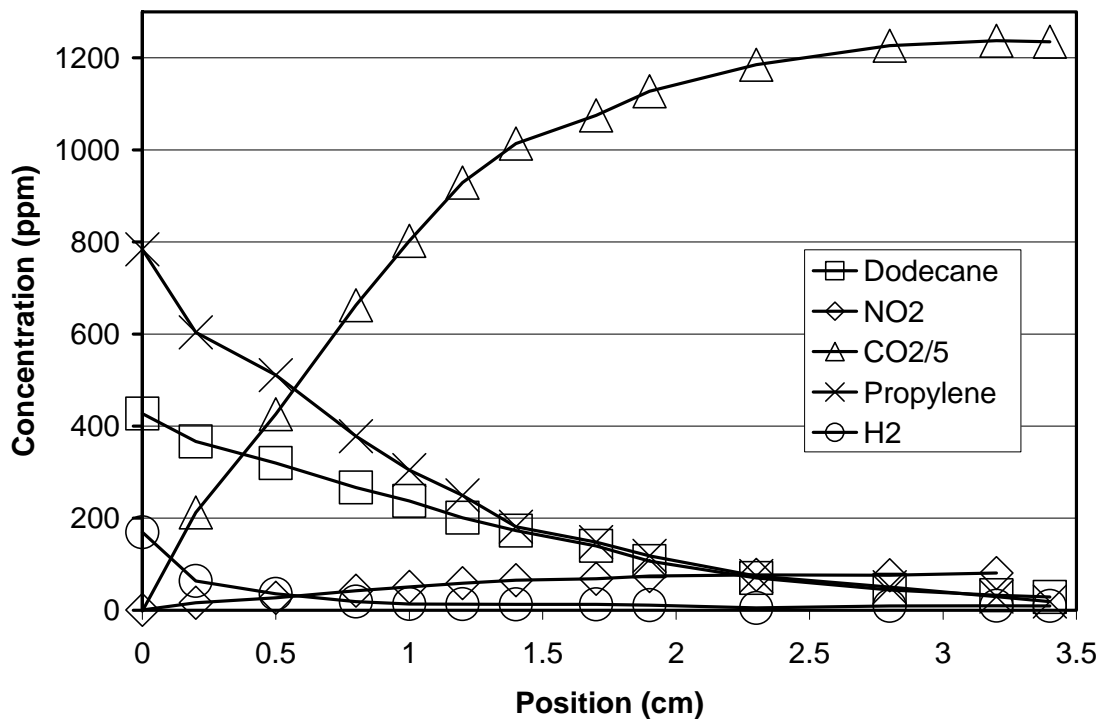
Figure 5-5: $C_{12}H_{26}$, NO_2, CO_2, C_3H_6 and H_2 concentrations as a function of position within the catalyst at an upstream temperature of 290°C.

At 248 and 290°C, the amount of CO_2 measured does not close a mass balance for the amount of hydrocarbon and CO reacted. However, once hydrocarbon oxidation began at these temperatures, CO formation and evidence of $C_{12}H_{26}$ partial oxidation products, such as aldehydes, were observed with the downstream FTIR analyzer. For example, ~115 ppm CO was seen at high temperatures where hydrocarbon oxidation was almost complete, along with ~60 ppm HCHO and ~20 ppm CH_3CHO. Therefore, even though the entire CO (800 ppm) fed into the system was oxidised at these temperatures, some CO is observed, but this CO comes from the partial oxidation of the hydrocarbon species and should not be linked with the lack of complete oxidation of feed stream CO. The presence of these partial combustion products help close the C mass balance.

Once oxidation began for a certain species, with every increase in temperature, light off for that species shifted to a position closer to the catalyst inlet. Such data demonstrate that ignition followed a back-to-front pattern typical of oxidation reactions under these conditions. In comparing the data obtained at the lower temperatures, Figures 5-2 and 5-3, all the observed CO_2 comes from CO oxidation since hydrocarbon oxidation began at temperatures greater than 208°C. The downstream FTIR verified the outlet CO concentrations, lending further confidence to the reported mass spectrometer results. At these low temperatures, an increase in CO_2 concentration was accompanied by a corresponding decrease in H_2 concentration. These changes occurred simultaneously with no observable difference in the light-off temperatures of CO and H_2. This does not however preclude that one species lit-off prior to the other, as these data were taken after steady-state was achieved.

A larger temperature rise was observed when hydrocarbon oxidation began, compared to the 5 and 15°C rise observed when just CO and H_2 were oxidizing. This relative difference in temperature rise is due to the larger amounts of hydrocarbons added. For example, there was a 120 and 140°C temperature rise across the catalyst during the experiments with upstream temperatures of 248 and 290°C respectively, where most of the hydrocarbons had oxidized. The generated exotherm caused hydrocarbon light-off to occur over a narrower temperature range. For example, H_2 oxidation began between 128 and 168°C. As shown in Figure 5-6, H_2 oxidation occurs in the downstream half of the catalyst at 168°C, with the oxidation occurring closer to the inlet with successive increase in temperature. H_2 oxidation only attains a steady profile between

43

248 to 290°C. However, C_3H_6 oxidation began at a higher temperature, somewhere between 208 and 248°C, and was almost completely oxidized with no significant change in the concentration profile between 248 and 290°C. Note: the C_3H_6 concentration is divided by 2 in the data shown in Figure 5-6.
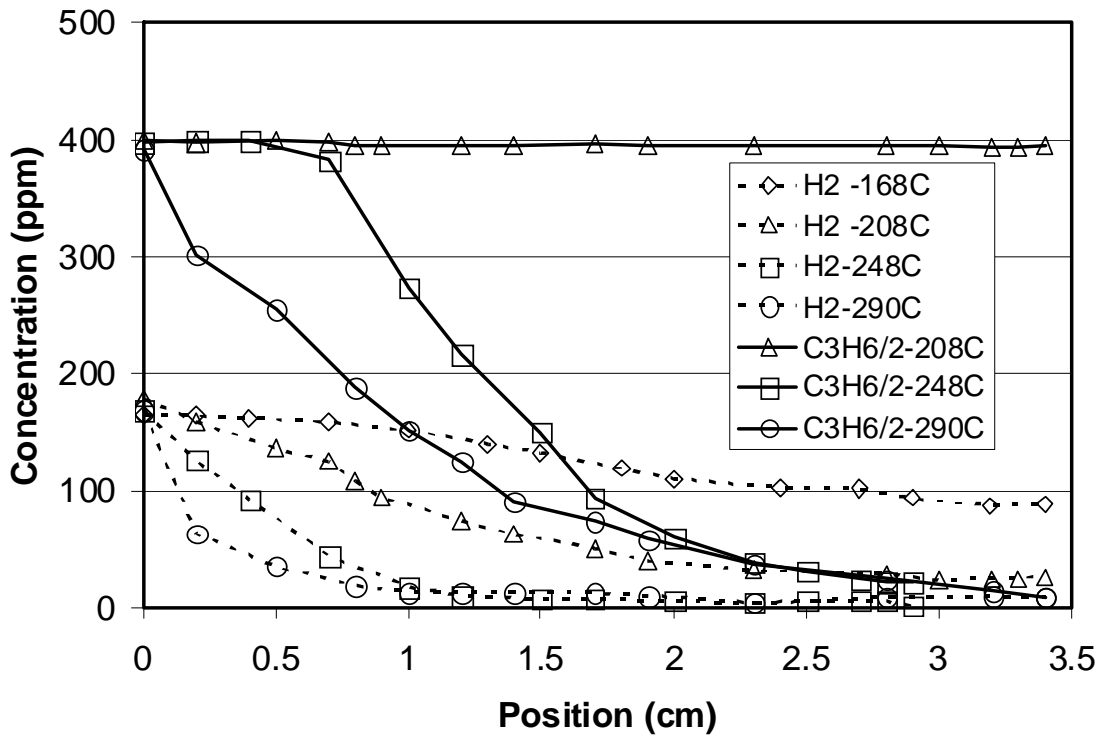
Figure 5-6: H_2 and C_3H_6 concentrations as a function of position and temperature within the catalyst.

The NO_2 concentration profiles at the various test temperatures are plotted in Figure 5-7. At 128°C, there was no NO oxidation and hence there is no NO_2 evident along the length of the catalyst. At 168°C, a small amount of NO oxidation is noted between ~1.3 and 2 cm with a slightly higher conversion observed between ~0.7 and 1.9 cm at 208°C, producing about 10 ppm of NO_2. At 248°C, significant NO to NO_2 conversion was observed, starting between approximately 0.7 and 2.3 cm while at 290°C oxidation occurred between ~0 and 1.9 cm.
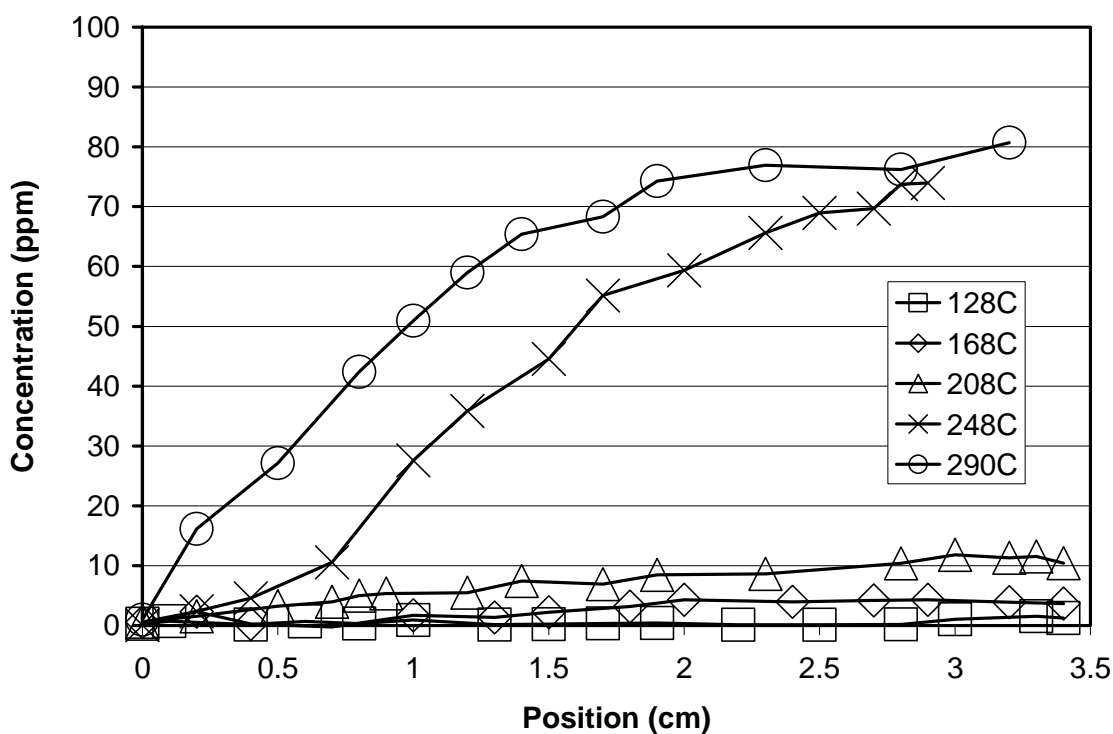
Figure 5-7: NO$_2$ concentration as a function of position and temperature within the catalyst.

The significant increase in NO$_2$ concentration was observed at the same temperature as hydrocarbon light off i.e. between 208 and 248°C, indicating that the hydrocarbon species influence NO oxidation, as discussed previously in Chapter 2, the literature review [75-80]. Furthermore, the measured NO conversion is higher than that typically seen over commercial DOC catalysts, which likely contain even higher precious metal levels. The results discussed in the previous chapter (Chapter 4) demonstrate that the addition of propylene inhibits NO oxidation by promoting the reduction of the product NO$_2$ to NO. This therefore indicates that it must be the dodecane enhancing NO oxidation. Also, as discussed in the literature review section, Hammer et al. [80] found that using a non-thermal plasma and with the reactor above 300°C, high concentrations of

hydrocarbons in diesel exhaust enhanced NO oxidation, via generation of O-radicals, which formed peroxy-radicals upon reacting with hydrocarbon molecules. The NO oxidation enhancement described by Figure 5-7 seemingly contradicts the results obtained in Chapter 4 where dodecane was also found to inhibit NO oxidation. There are experiment details that explain this apparent contradiction. There were signs of an enhancement effect caused by dodecane beyond ~320°C in the data obtained for Chapter 4 (not shown in Figure 4-2); however, the enhancement seen in Figure 5-7 takes place at lower temperatures, between 208°C and 290°C, indicating that temperature was not the sole variable responsible for the enhancement. Experiments with various dodecane concentrations were carried out, with the results shown in Figure 5-8. NO oxidation was enhanced only with higher dodecane concentrations, 275 and 400 ppm in the data shown, and not by lower amounts (45 and 100 ppm). The experiment in Chapter 4 was conducted with 200 ppm $C_{12}H_{26}$ and thus there was still an inhibition, while the above experiments described in Figures 5-1 through 5-7 were performed with 425 ppm $C_{12}H_{26}$. It is speculated that the effect is due to dodecane partial oxidation products, and gas product analysis in the range where dodecane was being oxidized yielded evidence of aldehydes. Previous literature evidence also exists regarding aldehydes as partial oxidation products from dodecane oxidation [80]. However, separate experiments with formaldehyde and acetaldehyde added did not lead to NO oxidation promotion. It is possible that incomplete combustion is occurring either upstream or at positions within the front portion of the catalyst, producing products that enhance NO oxidation, but those products are consumed before exiting the reactor and therefore are not observed by the FTIR analyzer. To date, there is no clear evidence as to what causes this effect, but it is consistently observed.
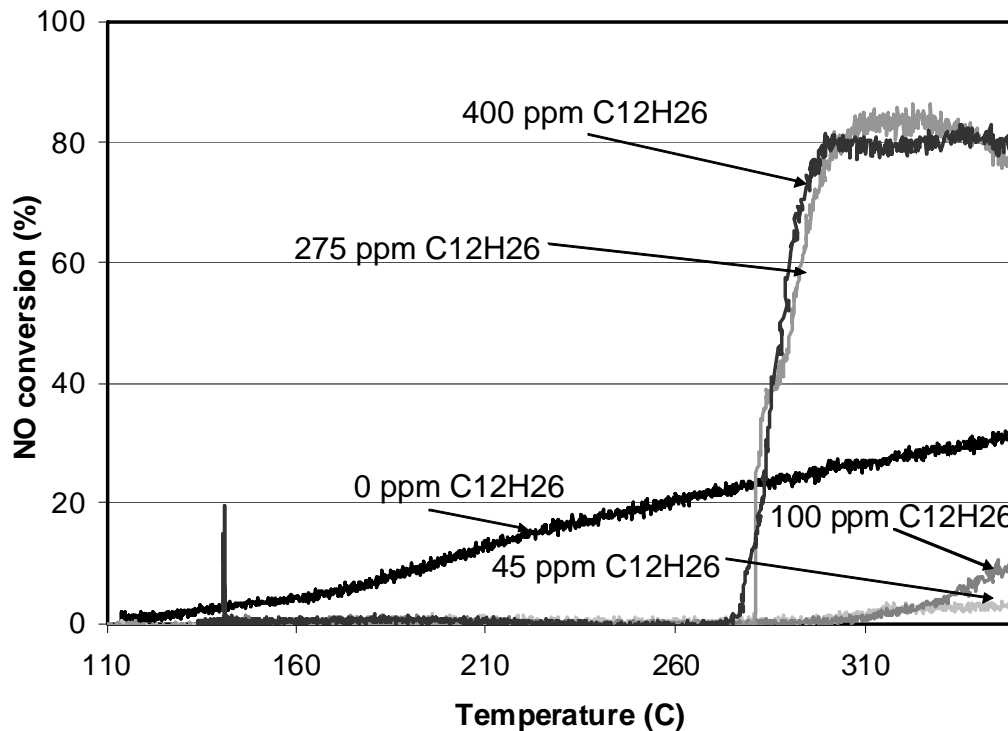
Figure 5-8: NO oxidation as a function of temperature and $C_{12}H_{26}$ concentration. The feed stream contained 100 ppm NO, 10% O_2, 5% H_2 with either 45, 100, 275 or 400 ppm $C_{12}H_{26}$ and a balance of N_2.

5.2 Temperature ramp experiments

The temperature ramp experiments were conducted with the capillary kept at a fixed position and the temperature ramped from about 120 to 400°C. After this the reactor was cooled, the capillary pulled to the next position and the experiment was repeated. Two different flow rates, corresponding to space velocities of 100,000 hr^{-1} and 52,500 hr^{-1}, were tested using this procedure. The feed stream composition was the same as that used in the "steady-state" experiments.

5.2.1 High flow rate experiments (space velocity = 100,000 hr^{-1})

For these experiments, the temperature was ramped at about 7.5°C/min with the capillary kept at fixed positions. The positions at which data were obtained were 0.875, 1.75 and 2.625 cm from the catalyst inlet as well as the capillary kept just at the outlet face of the catalyst.

The data obtained with the capillary at the outlet face of the catalyst are shown in Figure 5-9. The H_2 and CO are consumed at lower temperature than the propylene and dodecane, consistent with the results presented in the previous section. Furthermore, it is apparent that the propylene lights off at a slightly lower temperature than the dodecane. NO oxidation begins after CO oxidation ends, i.e. there is no CO remaining. This could be due to NO_2 being reduced to NO in the presence of CO, thus lowering the observed NO oxidation conversion, similar to the propylene oxidation mechanism presented in Chapter 4 [9,77]. Another possibility is that CO is initially adsorbed over the Pt surface, and once CO oxidation begins, Pt sites then become available for NO oxidation. Crocoll et al. [78] presented such a mechanism based on data from a Pt/Al_2O_3 catalyst where the oxidation rate of NO decreased significantly below 250°C in the presence of CO. As shown in Figure 5-9, the NO oxidation conversion increases significantly after 210°C, which is when dodecane oxidation began, once again indicating that dodecane enhanced NO oxidation, consistent with the data discussed previously in the "steady-state" experiments.
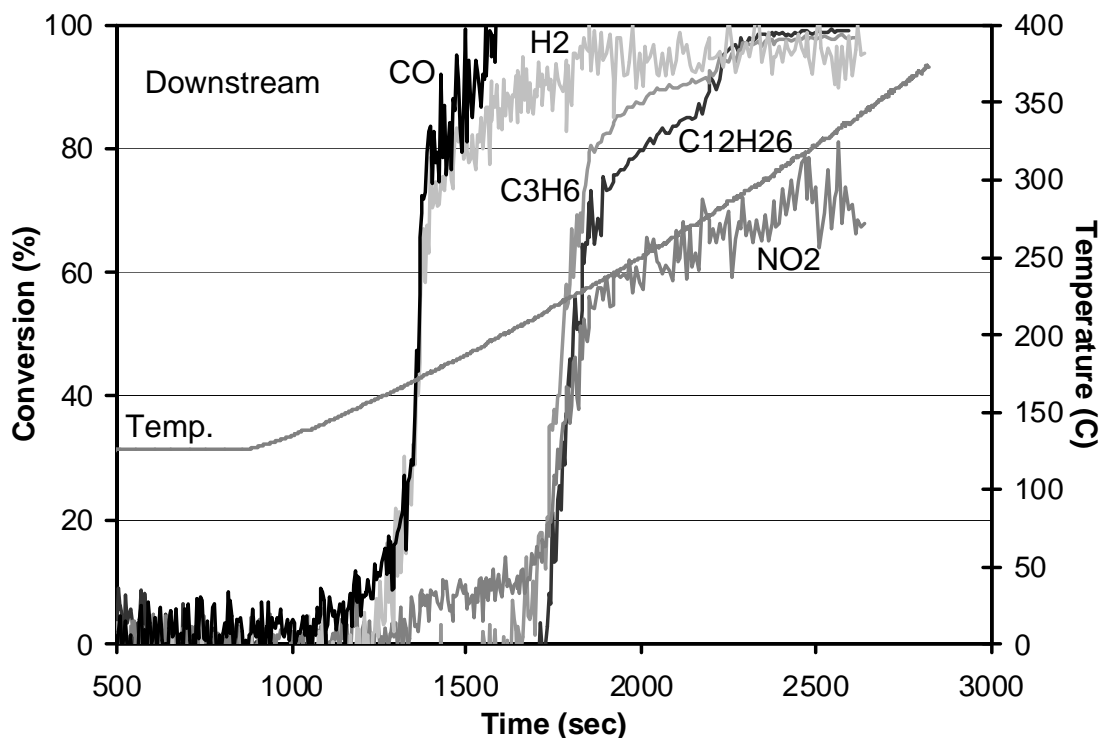
<u>Figure 5-9</u>: CO, H_2, C_3H_6, $C_{12}H_{26}$ and NO conversions as a function of time/temperature. These data were taken at the catalyst outlet.

In comparing the CO and H_2 conversions, it seems that after about 50% conversion, CO oxidation approaches full conversion more rapidly than H_2. This phenomenon is caused by the way the CO oxidation conversion was calculated. The mass spectrometer used in these experiments cannot distinguish between CO and N_2 because they both have the same molecular mass. Instead, CO_2 is measured and the CO conversion is based on CO_2 produced. However, CO_2 is also produced from hydrocarbon oxidation and thus contributes to the calculated amount once hydrocarbon oxidation begins. With this complication, CO conversion is plotted, but hydrocarbon oxidation may contribute to the calculated CO conversion at higher conversions (higher temperatures actually), while at lower conversion and temperature all the CO_2 comes from CO oxidation only.

The conversions as a function of time and temperature with the capillary at a distance of 2.625 cm from the catalyst inlet (0.375 cm upstream of the data shown in Figure 5-9) are shown in Figure 5-10. The same trends as those discussed above were observed at this position; where H_2 and CO oxidation take place before hydrocarbon oxidation and C_3H_6 oxidation begins prior to that of $C_{12}H_{26}$. As compared to the downstream position, the oxidation of all the species began later in time and at a slightly higher temperature. For example, the temperature to achieve 50% conversion of dodecane at the downstream position was ~226°C, while at 2.625 cm from inlet it was ~236°C. This, consistent with the data presented in section 5-1, indicates that a back-to-front ignition pattern occurred.
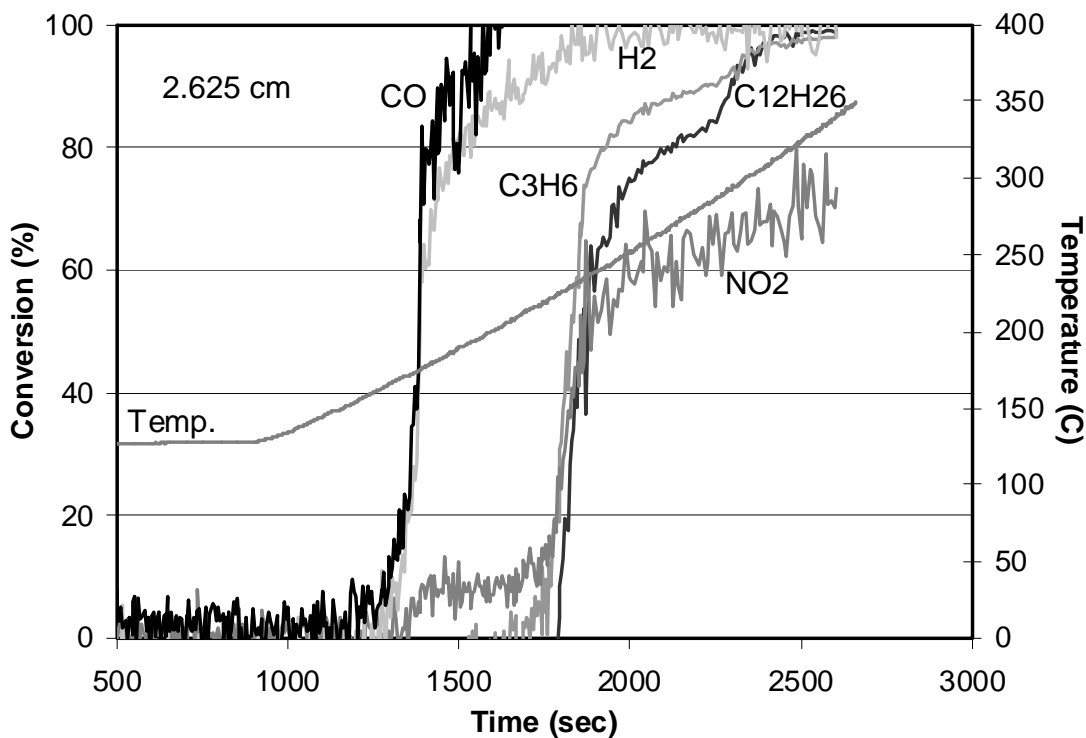

Figure 5-10: CO, H_2, C_3H_6, $C_{12}H_{26}$ and NO conversions as a function of time/temperature. These data were taken at 2.625 cm from the catalyst inlet.

Figure 5-11 shows the conversions obtained with the capillary at 1.75 cm from the catalyst inlet (the midpoint of the catalyst). Once again, the hydrocarbons oxidize after CO and H_2. 50% dodecane conversion was obtained at ~245°C, which is higher than that obtained at 2.625 cm and the outlet by about 11 and 21°C respectively.

Figure 5-11: CO, H_2, C_3H_6, $C_{12}H_{26}$ and NO conversions as a function of time/temperature. These data were taken at 1.75 cm from the catalyst inlet.

The last position tested was 0.875 cm from the catalyst inlet, the data for which is shown in Figure 5-12. At this position too, all the species followed the same trends as seen earlier. They began oxidizing later in time and at a higher temperature than that observed at the downstream positions of the catalyst. At 0.875 cm from the inlet, the dodecane conversion reaches 50% at ~292°C, indicating that in order to achieve the same conversion as that attained at the midpoint of the catalyst, the temperature must be raised by 47°C.
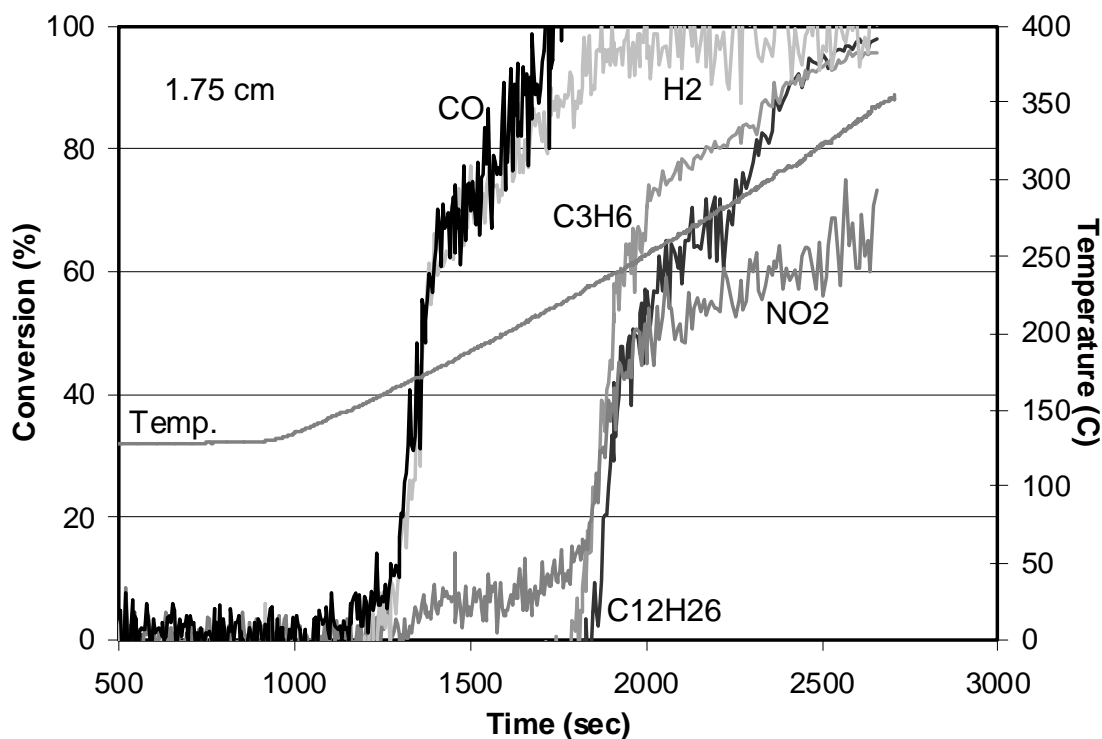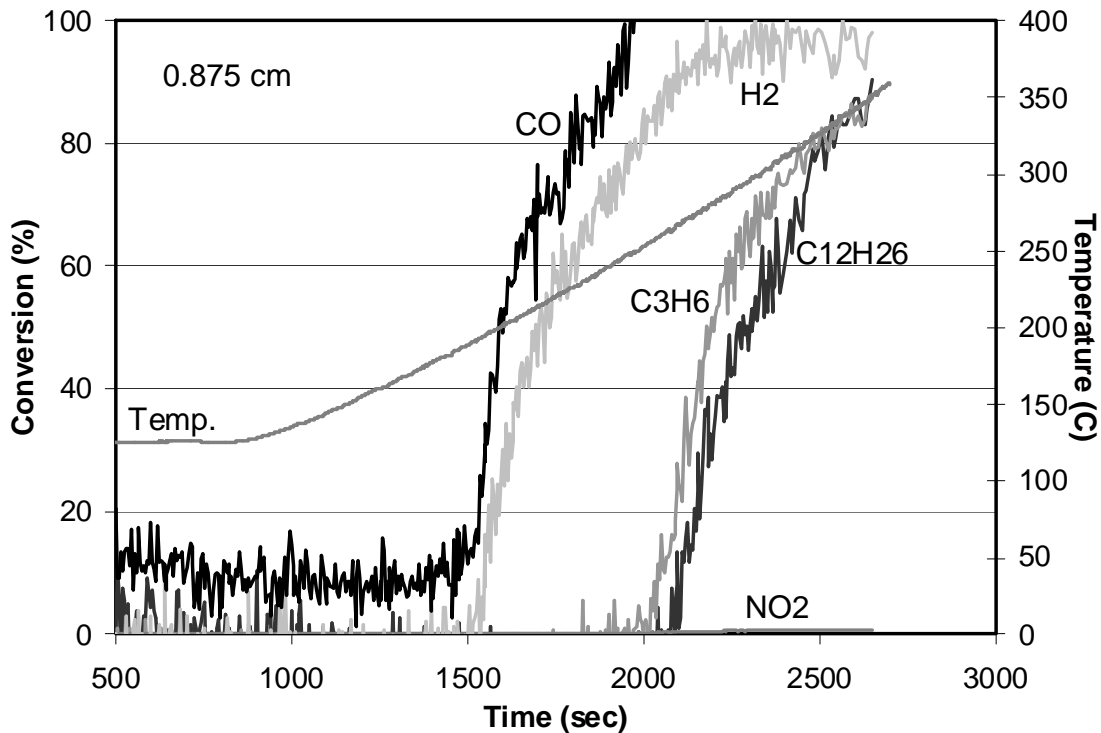
Figure 5-12: CO, H$_2$, C$_3$H$_6$, C$_{12}$H$_{26}$ and NO conversions as a function of time/temperature. These data were taken at 0.875 cm from the catalyst inlet.

Table 5-1 summarizes the temperatures required to obtain 50% conversion of H$_2$, C$_3$H$_6$ and C$_{12}$H$_{26}$ at each position. At each position, H$_2$ oxidation began first followed by C$_3$H$_6$ and C$_{12}$H$_{26}$ oxidation. Also, the oxidation of each began at the catalyst outlet and progressively required a higher temperature to achieve 50% conversion as the capillary was placed closer to the catalyst inlet. A back-to-front ignition pattern is caused by heat generated via the exothermic reaction initially being transferred down the monolith from the upstream positions via conduction and convection. This heat, or increase in temperature, results in more oxidation, and therefore the rate of oxidation typically increases down the length of the catalyst. Thus, before light-off the catalyst is hottest at the downstream position. At some temperature, light-off begins and progressively moves

52

to the upstream positions. This upstream movement is from heat now being conducted

upstream, since there is, after light-off, a higher temperature at the back of the monolith.

	Temperature for 50% conversion (T_{50})		
Position	H_2	C_3H_6	$C_{12}H_{26}$
Downstream	174	223.5	226°C
2.625 cm	175.5	230	236°C
1.75 cm	176	240	245°C
0.875 cm	216	281.5	292°C

Table 5-1: Temperature for 50% conversion of H_2, C_3H_6 and $C_{12}H_{26}$ at the various catalyst positions.

The data did not show a significant difference in the H_2 and CO light-off. However, in each of the data sets, it appears that CO_2 production began just prior to the start of H_2 consumption. Although the above results suggest that CO light-off occurs slightly before H_2 oxidation, it is not considered conclusive proof at this stage due to the marginal difference.

The results also show that the progression of the CO and H_2 oxidation fronts through the catalyst are faster than that of the hydrocarbon oxidation fronts. This is highlighted by comparing the H_2 and propylene conversions from Figures 5-13 and 5-14 respectively. H_2 oxidation (Figure 5-13) begins at the downstream position at about 1240 seconds. This oxidation front then progressively travels towards the inlet of the catalyst. Closest to the catalyst inlet (at 0.875 cm from the inlet), H_2 light-off begins at ~1500 seconds, therefore taking 260 seconds to travel from the downstream position to 0.875 cm from the inlet. In contrast, propylene oxidation began at the downstream position as

well (Figure 5-14), however at a much later time, approximately 1665 seconds and oxidation began at 0.875 cm from the inlet at ~2000 seconds. The propylene oxidation front travelled from the catalyst outlet to 0.875 cm in ~335 seconds.

Thus, by comparing the temperatures for 50% conversion of H_2 and C_3H_6 from Table 5-1 and the results shown in Figures 5-13 and 5-14, not only did C_3H_6 oxidation begin after H_2 oxidation at each position, but also took a longer time for its oxidation front to travel from the catalyst outlet to the inlet. This is likely due to the higher temperature necessary for propylene oxidation light off and extra energy required for its conversion as well as heat transfer and capacity differences between the species [88].
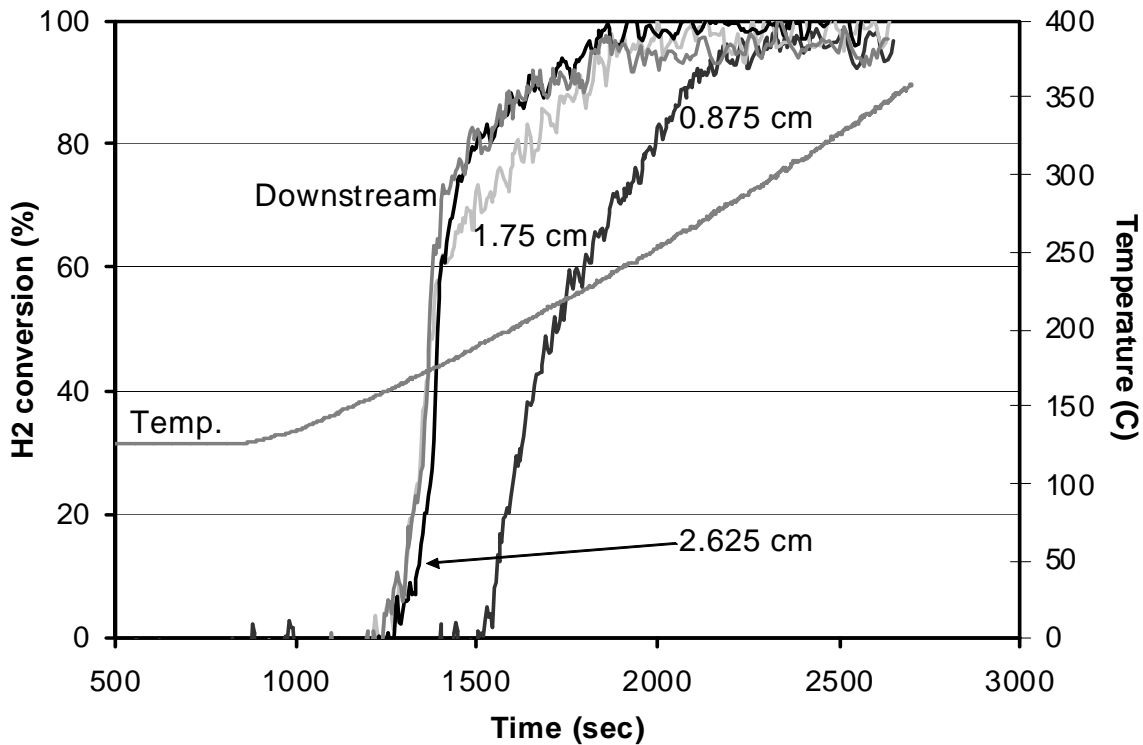

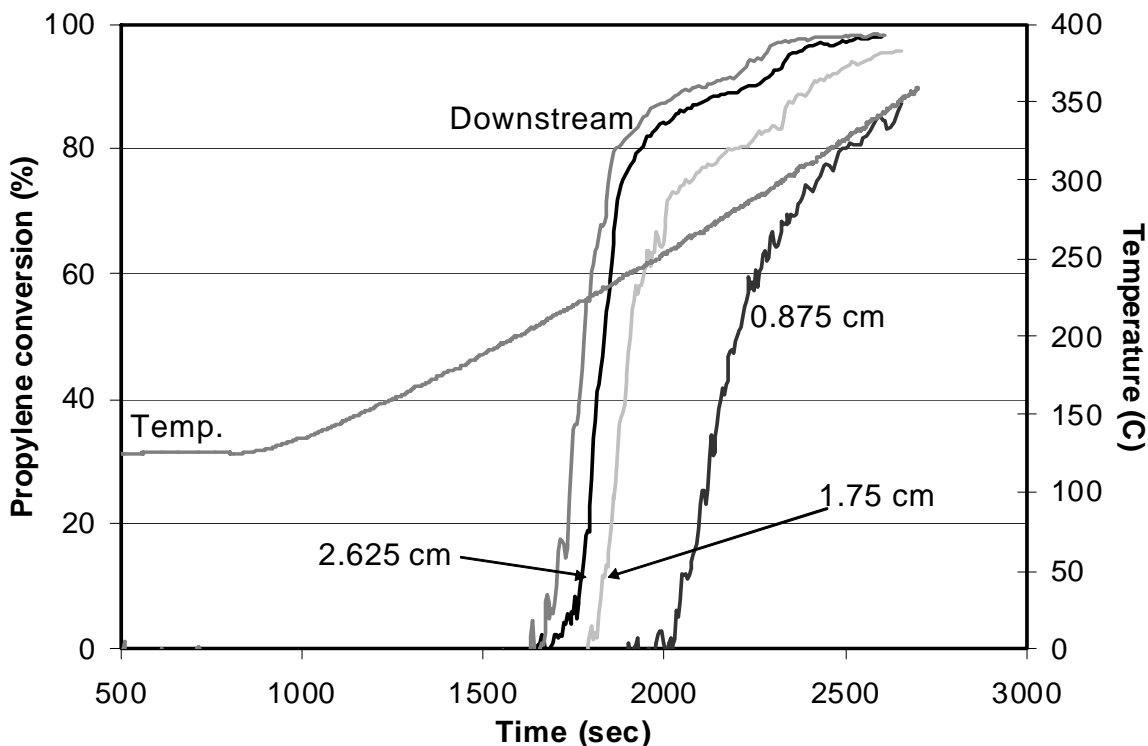Figure 5-13: H_2 conversion as a function of catalyst position.

Figure 5-14: C_3H_6 conversion as a function of catalyst position.

5.2.2   Low flow rate experiments (space velocity = 52,500 hr^{-1})

These experiments were also conducted with the capillary placed at 0.875, 1.75 and 2.625 cm from the catalyst inlet and at the outlet face of the catalyst. The temperature was ramped at 8.1°C/min at each of these positions. Again, the CO conversions were calculated based on measured CO_2, and therefore after hydrocarbon oxidation begins plotted CO conversions are influenced by hydrocarbon oxidation. Figure 5-15 shows the data obtained with the capillary at the catalyst outlet. CO and H_2 light-off began at a lower temperature than C_3H_6 oxidation which began prior to $C_{12}H_{26}$ oxidation. There was no observable difference between CO and H_2 oxidation under these conditions. Also, NO oxidation was inhibited below 200°C and accelerated above ~210°C once $C_{12}H_{26}$ oxidation began. This once again suggests that dodecane is enhancing NO oxidation through the possibilities discussed in section 5.1.
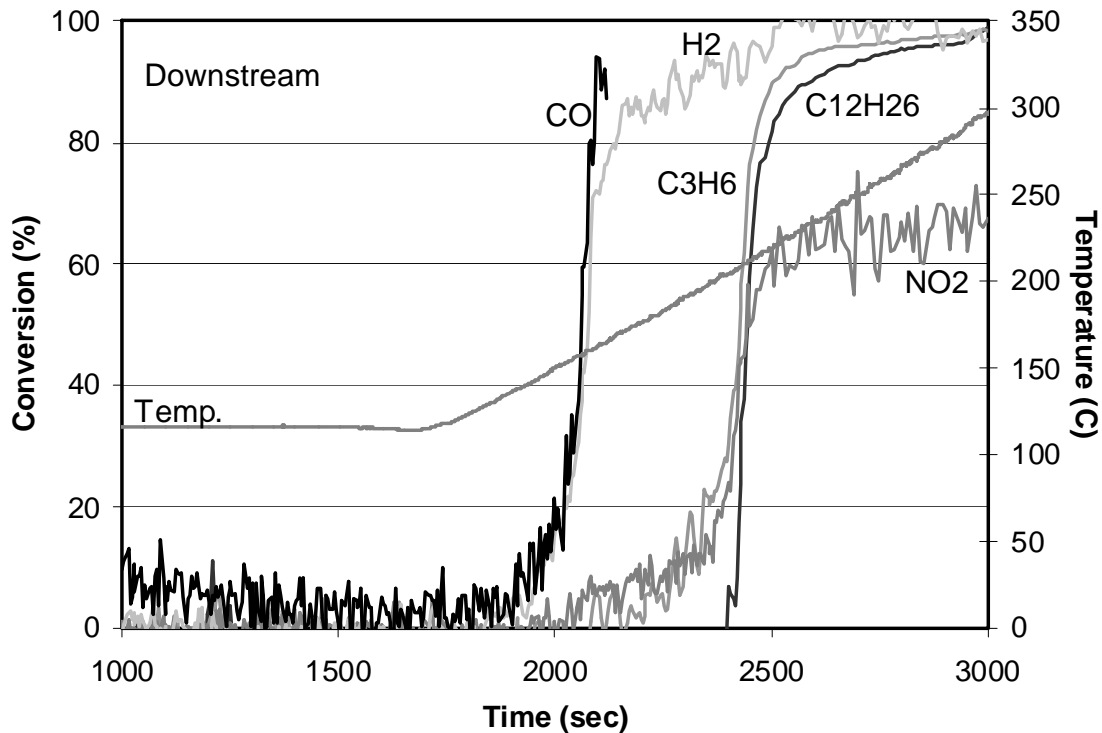
Figure 5-15: CO, H_2, C_3H_6, $C_{12}H_{26}$ and NO conversions as a function of time/temperature. These data were taken at the catalyst outlet.

The data obtained at 2.625 cm from the catalyst inlet are shown in Figure 5-16. CO and H_2 oxidation began at a slightly later time and at a higher temperature than that at the catalyst outlet, indicating that after beginning at the outlet, their oxidation fronts moved closer to the inlet of the catalyst. However, the hydrocarbon oxidation data show that they began oxidizing at the same time as that observed in Figure 5-15. This indicates that the hydrocarbons did not follow a back-to-front oxidation pattern under these lower flow conditions. The reason for such behaviour will be discussed later.
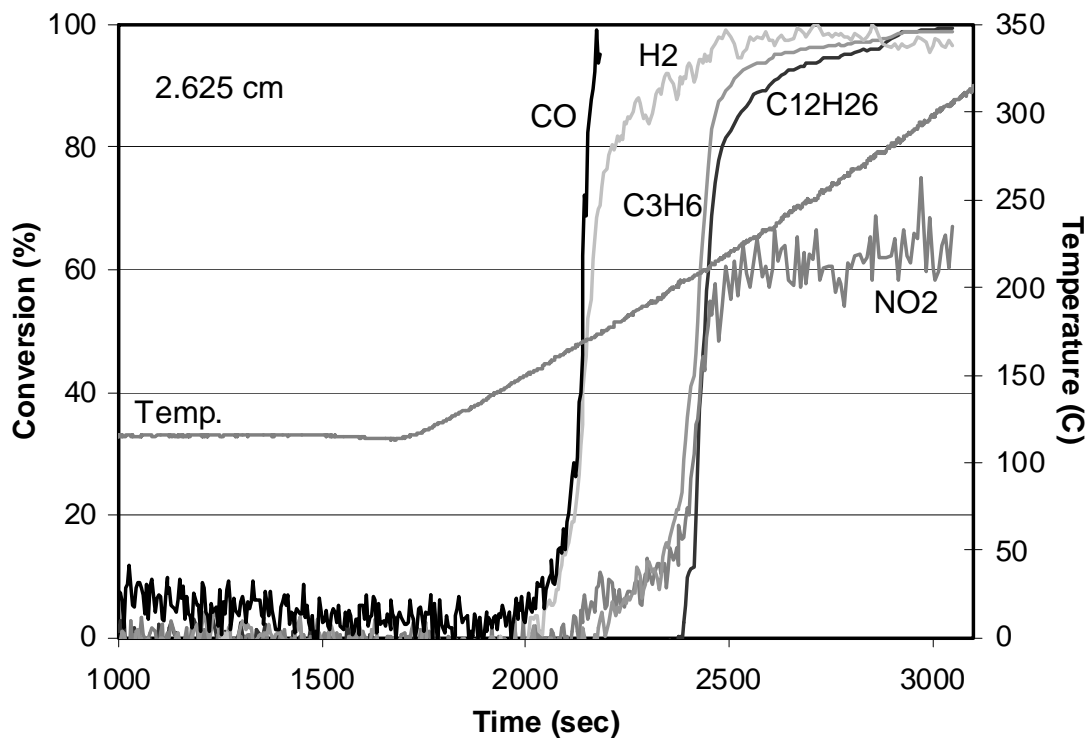
<u>Figure 5-16</u>: CO, H_2, C_3H_6, $C_{12}H_{26}$ and NO conversions as a function of time/temperature. These data were taken at 2.625 cm from the catalyst inlet.

The next position tested was at the midpoint of the catalyst, with the data shown in Figure 5-17. Once again CO and H_2 light-off occurred earlier than hydrocarbon oxidation, with no observable difference in their light-off times. Light off occurred at a slightly higher temperature and later time compared to downstream positions. Also again, C_3H_6 and $C_{12}H_{26}$ oxidation began at the same time as that seen at the outlet and at 2.625 cm from the inlet. Here too significant NO_2 production was seen at temperatures > 210°C, due to dodecane enhancement.
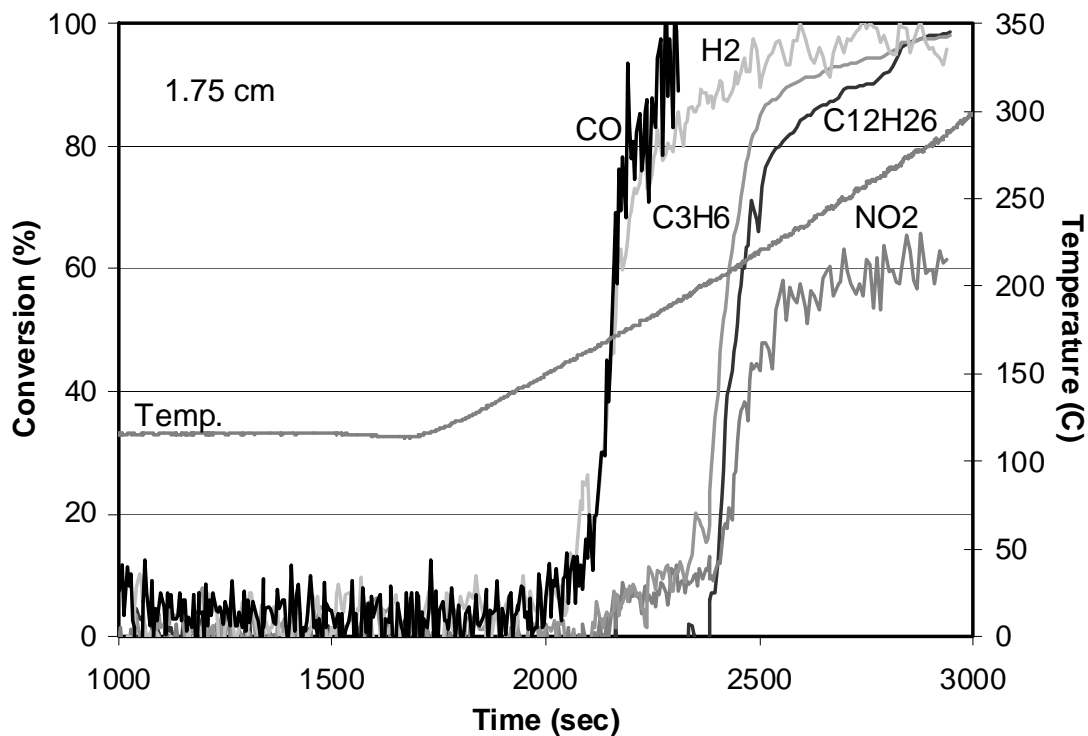
Figure 5-17: CO, H$_2$, C$_3$H$_6$, C$_{12}$H$_{26}$ and NO conversions as a function of time/temperature. These data were taken at 1.75 cm from the catalyst inlet.

At 0.875 cm from the catalyst inlet (Figure 5-18), CO and H$_2$ oxidation began at a higher temperature and was also observed later compared to the downstream positions. At this upstream position, the back-to-front oxidation trend seen for CO and H$_2$ was here also observed for the hydrocarbons, as C$_3$H$_6$ and C$_{12}$H$_{26}$ light-off occurred at a later time and higher temperature compared to the data from the downstream positions.
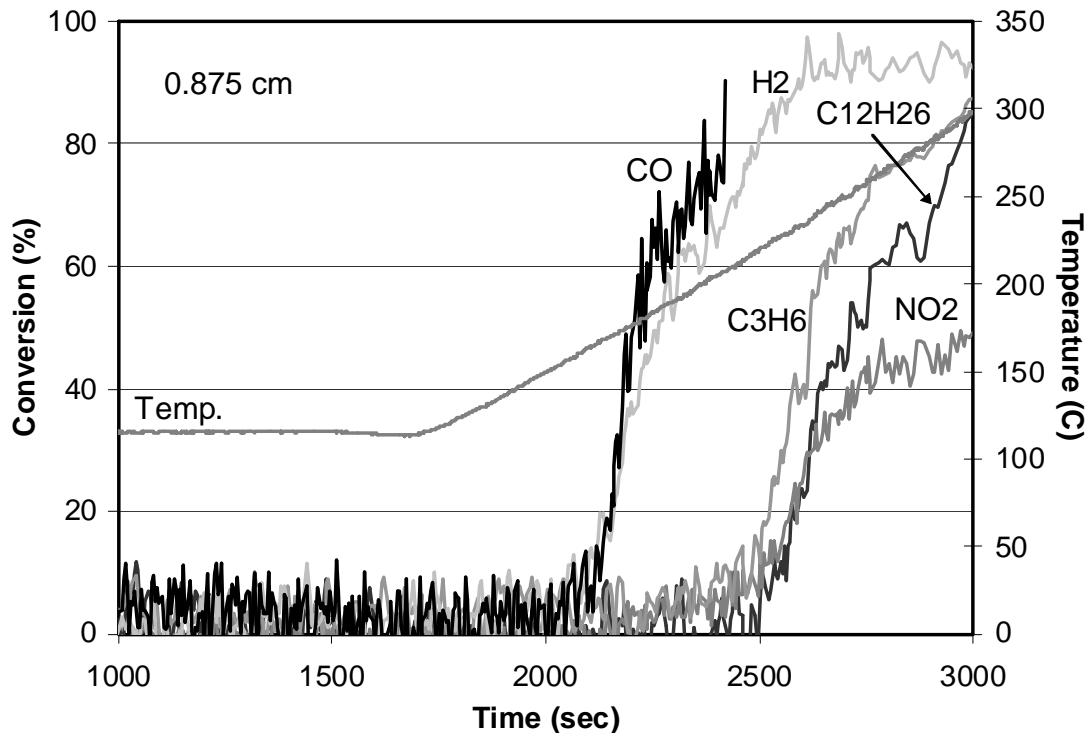
Figure 5-18: CO, H_2, C_3H_6, $C_{12}H_{26}$ and NO conversions as a function of time/temperature. These data were taken at 0.875 cm from the catalyst inlet.

Similar to the higher flow rate experiments discussed in section 5.2.1, the results in this case also showed a faster movement of the CO and H_2 oxidation fronts through the catalyst as compared to the hydrocarbons. However, unlike the high flow rate case, hydrocarbon oxidation did not begin at the back of the sample, but towards the middle. This is highlighted in Figure 5-19 where the C_3H_6 oxidation profile as a function of time and temperature is identical for all positions downstream of 0.875 cm. The oxidation front still followed the back-to-front movement, but it began in the middle of the catalyst (1.75 cm from the inlet), instead of at the outlet face as it did with the higher flow rate. Dodecane followed a trend similar to propylene. The reason for such trends shown by the hydrocarbons is discussed below based on the results obtained by Yakhin & Menzinger [88].

59

As the temperature increases, it accelerates the oxidation of the reactant species, here all of which are exothermic reactions. The heat released from any extent of reaction is carried downstream through conduction and convection. At incomplete conversions, or more specifically, when the reaction is spread through the catalyst prior to light off, the back of the sample will be relatively hotter than the front. Once light-off occurs at the back of the catalyst, conduction along the monolith from the hotter region will now cause the reaction front to move upstream as the heat will transfer from the hotter spot to cooler. With high flow rates hydrocarbon oxidation began at the outlet, matching this logic. Also, at high gas flow rates, less time is available for the gas to remain in contact with the monolith walls, lowering the gas temperature compared to the walls where the reaction is occurring. In the case of the low flow rates, the gas residence time is increased, allowing it to exchange more heat with the catalyst. Under certain conditions the gas is hotter than the catalyst walls via convection from upstream hot regions. Some of the heat generated by the exothermic H_2 and CO reactions is transferred to the gas through convection and carried away by it. The data therefore suggest that the heat from the CO and H_2 reactions, as well as some contribution from a small extent of propylene and dodecane oxidation, is sufficient to warm the middle of the catalyst enough to induce hydrocarbon oxidation. Whereas with the higher flow rate experiments, convective heat transfer was larger, and took heat away from the solid at a higher rate so that the heat from propylene and dodecane oxidation needed to build through the entire catalyst, on top of that generated from CO and H_2 oxidation, for light off to begin.
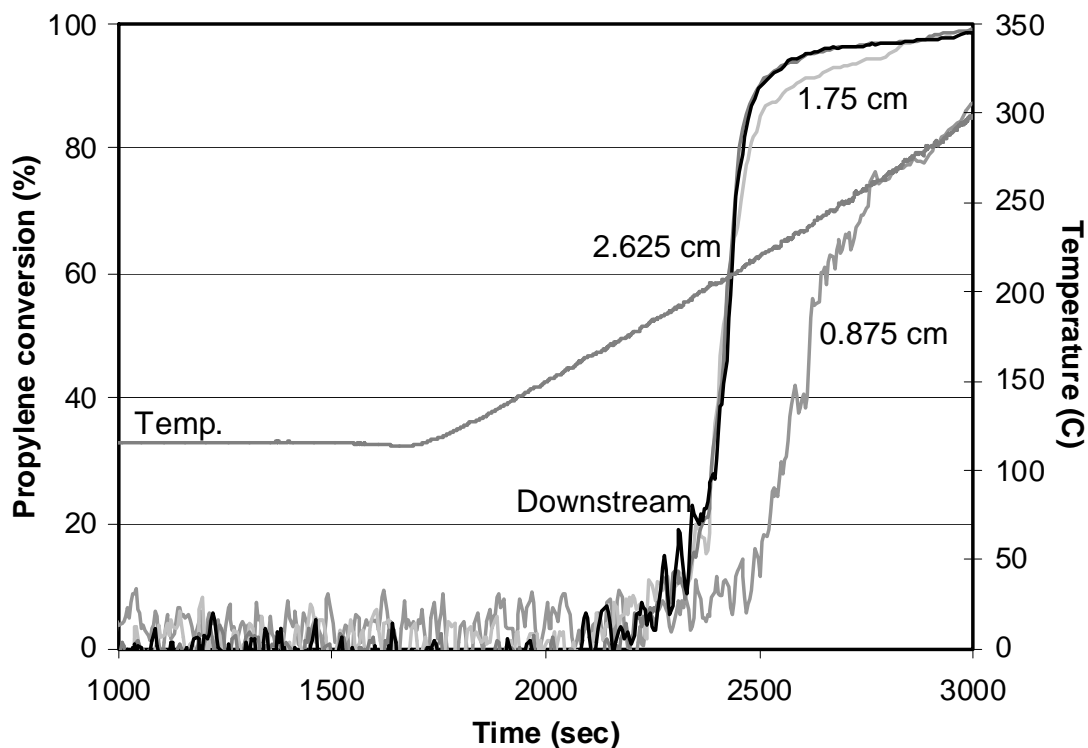
Figure 5-19: C_3H_6 conversion as a function of catalyst position.

Spatially resolving the oxidation reactions along the length of the catalyst showed that all species followed a back-to-front ignition pattern with oxidation first observed at the downstream of the catalyst, except in the case of hydrocarbons with low gas flow rate where oxidation of the species began in the middle of the catalyst. CO and H_2 oxidation began before C_3H_6 oxidation which in turn began prior to $C_{12}H_{26}$ oxidation. Also, the CO and H_2 oxidation front moved through the catalyst at a faster rate than the hydrocarbons for both high and low flow rates.

Conclusions

Competitive oxidation reactions exist over a model $Pt-Pd/Al_2O_3$ monolithic diesel oxidation catalyst and various components of diesel exhaust affect the oxidation rates of one another. As part of this study, the effect of various hydrocarbons on NO oxidation was evaluated. Propylene had an apparent inhibition effect on NO oxidation due to NO_2, the product of NO oxidation, being used as a reactant in propylene oxidation. This was verified by experiments with NO_2 in the feed instead of NO, which showed that NO_2 reduction was faster and occurred at lower temperatures in the presence of propylene. Similar results were obtained with m-xylene and dodecane addition. Conversely, the results showed that a feed stream consisting of NO_2 along with low O_2 concentrations had an apparent inhibition effect on propylene oxidation once NO_2 reduction began, and this was due to the NO formed. Therefore, not only does propylene consume NO_2 and inhibit NO oxidation, but NO also inhibits propylene oxidation.

The SpaciMS technique was used to understand the distribution of the reactant and product gas species at different positions within the catalyst both at constant and varying temperatures. The results showed that CO and H_2 oxidation always began before C_3H_6 oxidation which was followed by $C_{12}H_{26}$ oxidation. All the species began oxidizing at the back of the catalyst, except in the case of low gas flow rates where the hydrocarbons lit-off in the middle of the sample. Oxidation then progressively moved closer to the inlet of the catalyst, following a back-to-front ignition pattern. The significant increase in NO_2 concentration observed at the start of hydrocarbon oxidation is related to an enhancement effect caused by dodecane, likely related to dodecane partial oxidation products.

Recommendations

- Conduct experiments with different combinations and concentrations of hydrocarbons to understand how they influence each others oxidation rates.

- Understand the influence of different precious metal loadings on the catalyst performance by conducting similar experiments on catalysts with different Pt-Pd ratios and comparing the results to the current project.

- Perform experiments with different concentrations and combinations of NO, dodecane and aldehydes to understand how dodecane enhances NO oxidation.

- Study the effects of thermal degradation on the performance of the catalyst.

- Employ an automated mechanism to pull the capillary to various positions within the catalyst.

- Insert more thermocouples at various positions along the length of the catalyst to get a better idea of the temperature changes within the monolith.

- Achieve better temperature monitoring and thus better control by setting up more thermocouples at various positions along the heated lines.

References

1. www.AVL.com

2. K. Schindler, SAE Technical Paper Series 972684.

3. S. Cho, Chemical Engineering Progress 90(1994)39.

4. A. Kato, S. Matsuda, T. Kamo, F. Nakajima, H. Kuroda and T. Narita, Journal of Physical Chemistry 85(1981)4099.

5. W. Majewski and M. Khair, Diesel Emissions and Their Control, SAE International, 2006.

6. W. Strehlau, U. Goebel, E. Lox, W. Mueller and R. Domesle, European Patent Application, EP 0 945 608 A2 (Degussa), 1999.

7. M. Brogan, A. Clark, and R. Brisley, SAE Technical Paper Series 980933.

8. S. Erkfeldt, M. Larsson, H. Hedblom and M. Skoglundh, SAE Technical Paper Series 1999-01-3504.

9. S. Erkfeldt, E. Jobson and M. Larsson, Topics in Catalysis 16/17(2001)127.

10. F. Rodrigues, L. Juste, C. Potvin, J.F. Tempere, G. Blanchard and G. Djega-Mariadassou, Catalysis Letters 72(2001)59.

11. N. Cant and M. Patterson, Catalysis Today 73(2002)271.

12. S. Hodjati, P. Bernhardt, C. Petit, V. Pitchon and A. Kiennemann, Applied Catalysis B: Environmental 19(1998)209.

13. S. Hodjati, K. Vaezzadeh, C. Petit, V. Pitchon and A. Kiennemann, Catalysis Today 59(2000)323.

14. W. Epling, L. Campbell, A. Yezerets, N. Currier and J. Parks, Catalysis Reviews 46(2004)163.

15. K. Kabin, R. Muncrief, M. Harold and Y. Li, Chemical Engineering Science 59(2004)5319.

16. S. Salasc, M. Skoglundh and E. Fridell, Applied Catalysis B: Environmental 36(2002)145.

17. H. Mahzoul, J.F. Brilhac and P. Gilot, Applied Catalysis B: Environmental 20(1999)47.

18. F. Prinetto, G. Ghiotti, I. Nova, L. Lietti, E. Tronconi and P. Forzatti, Journal of Physical Chemistry B 105(2001)12732.

19. S. Kikuyama, I. Matsukuma, R. Kikuchi, K. Sasaki and K. Eguchi, Applied Catalysis A: General 226(2002)23.

20. P. Schmitz and R. Baird, Journal of Physical Chemistry B 106(2002)4172.

21. J. Jung, S. Song and K. Min Chun, SAE Technical Paper Series 2008-01-0482.

22. C. Lambert, R. Hammerle, R. McGill, M. Khair and C. Sharp, SAE Technical Paper Series 2004-01-1292.

23. www.dieselnet.com

24. A. Neyestanaki, F. Klingstedt, T. Salmi and D. Murzin, Fuel 83(2004)395.

25. M. Chen and L. Schmidt, Journal of Catalysis 56 (1979) 198.

26. A. Morlang, U. Neuhausen, K. Klementiev, F. Schütze, G. Miehe, H. Fuess and E. Lox, Applied Catalysis B: Environmental 60(2005)191.

27. J. Andersson, M. Antonsson, L. Eurenius, E. Olsson and M. Skoglundh, Applied Catalysis B: Environmental 72(2007)71.

28. J. Sinfelt, G. Via and F. Lytle, Journal of Chemical Physics 72(1980)4832.

29. T. Rades, C. Pak, M. Polisset-Thfoin, R. Ryoo and J. Fraissard, Catalysis Letters 29(1994)91.

30. K. Bae and M. Chang, SAE Technical Paper Series 943929.

31. A. Aitken, W. Southgate, R. Cawdell and P.Shore, SAE Technical Paper Series 964322.

32. K. Voss, J. Cioffi, A. Gorel, M. Norris, T. Rotolico and A. Fabel, SAE Technical Paper Series 970469.

33. E. Dawson and J. Kramer, SAE Technical Paper Series 2006-01-1525.

34. K. Voss, J. Adomaitis, R. Feldwisch, C. Borg, E. Karlsson and B. Josefsson, SAE Technical Paper Series 950155.

35. A. Ayala, M. Gebel, R. Okamoto, P. Rieger, N. Kado, C. Cotter and N. Verma, SAE Technical Paper Series 2003-01-1900.

36. K. Fujdala, T. Truex, J. Nicholas and J. Woo, SAE Technical Paper Series 2008-01-0070.

37. T. Watanabe, K. Kawashima, Y. Tagawa, K. Tashiro, H. Anoda, K. Ichioka, S. Sumiya and G. Zhang, SAE Technical Paper Series 2007-01-1920.

38. P. Blakeman, A. Chiffey, P. Phillips, M. Twigg and A. Walker, SAE Technical Paper Series 2003-01-3753.

39. L. Olsson, B. Westerberg, H. Persson, E. Fridell, M. Skoglundh and B. Andersson, Journal of Physical Chemistry B 103(1999)10433.

40. S. Mulla, N. Chen, W. Delgass, W. Epling and F. Ribeiro, Catalysis Letters 100(2005)267.

41. S. Mulla, N. Chen, L. Cumaranatunge, G. Blau, D. Zemlyanov, W. Delgass, W. Epling and F. Ribeiro, Journal of Catalysis 241(2006)389.

42. J. Després, M. Elsener, M. Koebel, O. Kröcher, B. Schnyder and A. Wokaun, Applied Catalysis B: Environmental 50(2004)73.

43. J. Segner, W. Vielhaber and G. Ertl, Israel Journal of Chemistry 22(1982)375.

44. D. Parker and B. Koel, Journal of Vacuum Science and Technology A 8(1990)2585.

45. G. Zheng and E. Altman, Surface Science 462(2000)151.

46. J. Lee and H. Kung, Catalysis Letters 51(1998)1.

47. E. Xue, K. Seshan and J. Ross, Applied Catalysis B: Environmental 11(1996)65.

48. P. Denton, A. Giroir-Fendler, H. Praliaud and M. Primet, Journal of Catalysis 189(2000)410.

49. L. Olsson and E. Fridell, Journal of Catalysis 210(2002)340.

50. S. Benard, L. Retailleau, F. Gaillard, P. Vernoux and A. Giroir-Fendler, Applied Catalysis B: Environmental 55(2005)11.

51. L. Olsson, M. Abul-Milh, H. Karlsson, E. Jobson, P. Thormaehlen and A. Hinz, Topics in Catalysis 30/31(2004)85.

52. P. Denton, A. Giroir-Fendler, H. Praliaud and M. Primet, Topics in Catalysis 16(2001)377.

53. V. Labalme, N. Guilhaume, E. Garbowski and M. Primet, Reaction Kinetics and Catalysis Letters 64(1998)207.

54. E. Putna, J. Vohs and R. Gorte, Surface Science 391(1997)L1178.

55. A. Ukharskii and A. Berman, Kinetics and Catalysis 33(1992)882.

56. A. Ukharskii and A. Berman, Kinetics and Catalysis 33(1992)888.

57. N. Tenyanko, Y. Sergeeva and N. Gaidai, Kinetics and Catalysis 31(1990)340.

58. A. Sinha and V. Shankar, Industrial and Engineering Chemistry Research 32(1993)1061.

59. J. Bart, A. Pentenero and M. Prigent, ACS Symposium Series 495(1992)42.

60. J. Bart, M. Prigent and A. Pentenero, Studies in Surface Science and Catalysis 96(1995)813.

61. I. Amon-Meziere, F. Castagna, M. Prigent and A. Pentenero, SAE Technical Paper Series 950932.

62. I. Mazzarino and A. Barresi, Catalysis Today 17(1993)335.

63. A. Barresi and G. Baldi, Industrial and Engineering Chemistry Research 33(1994)2964.

64. M. Patterson, D. Angove and N. Cant, Applied Catalysis B: Environmental 26(2000)47.

65. R. McCabe, W.O. Siegl, W. Chun and J. Perry, Journal of the Air and Waste Management Association 42(1991)1071.

66. N. Pelz, N. Dempster, G. Hundleby and P. Shore, SAE Technical Paper Series 902074.

67. W. Siegl, E. Kaiser, A. Adamczyk, M. Guenther, D. DiCicco and D. Lewis, SAE Technical Paper Series 982549.

68. G. Mabilon, D. Durand and P. Courty, Studies in Surface Science and Catalysis 96(1995)775.

69. S. Ordóñez, L. Bello, H. Sastre, R. Rosal and F. V. Diez, Applied Catalysis B: Environmental 38(2002)139.

70. A. Barresi and G. Baldi, Chemical Engineering Science 47(1992)1943.

71. S. Gangwal, M. Mullins, J. Spivey, P. Caffrey and B. Tichenor, Applied Catalysis 36(1988)231.

72. J. Hermia and S. Vigneron, Catalysis Today 17(1993)349.

73. B. Grbic, N. Radic and A. Terlecki- Baricevic, Applied Catalysis B: Environmental 50(2004)161.

74. P. Papaefthimiou, T. Ioannides and X. Verykios, Applied Catalysis B: Environmental 13(1997)175.

75. S. Voltz, C. Morgan, D. Liederman and S. Jacob, Industrial and Engineering Chemistry Product Research and Development 12(1973)294.

76. R. Burch and T.C. Watling, Catalysis Letters 43(1997)19.

77. S. Katare, J. Patterson and P. Laing, SAE Technical Paper Series 2007-01-3984.

78. M. Crocoll, S. Kureti and W. Weisweiler, Journal of Catalysis 229(2005)480.

79. S. Derrouiche and D. Bianchi, Journal of Catalysis 242(2006)172.

80. T. Hammer, T. Kishimoto, B. Krutzsch, R. Andorf, and C. Plog, SAE Technical Paper Series 2001-01-3567.

81. W. Partridge, J. Storey, S. Lewis, R. Smithwick, G. DeVault, M. Cunningham, N. Currier and T. Yonushonis, SAE Technical Paper Series 2000-01-2952.

82. B. West, S. Huff, J. Parks, S. Lewis, J. Choi, W. Partridge and J. Storey, SAE Technical Paper Series 2004-01-3023.

83. J. Choi, W. Partridge and C. Daw, Applied Catalysis A: General 293(2005)24.

84. J. Choi, W. Partridge, W. Epling, N. Currier and T. Yonushonis, Catalysis Today 114(2006)102.

85. J. Choi, W. Partridge and C. Daw, Applied Catalysis B: Environmental 77(2007)145.

86. J. Choi, W. Partridge, J. Pihl and C. Daw, Catalysis Today 136(2008)173.

87. W. Partridge, T. Toops, J. Green and T. Armstrong, Journal of Power Sources 160(2006)454.

88. V. Yakhnin and M. Menzinger, Chemical Engineering Science 57(2002)4559.

Appendices

Appendix A

A-1 Mass spectrometer calibration procedure

Partial pressures of the gas species, measured in torr, are obtained with the mass spectrometer. To convert these partial pressures to ppm or % values, the following calibration procedure was used.

First, the measured partial pressures of each gas were divided by the partial pressure of helium to obtain a ratio between them.

$$Ratio = Gas \ species \ (torr) \ / \ He \ (torr)$$

This ratio was then multiplied by the percentage of He entering the system. This provided the uncorrected, initial percentage of the gas species.

$$Uncorrected \ gas \ species \ (\%) = inlet \ He \ (\%) * ratio$$

The above calculation did not take into account the detector's relative sensitivity to different gas species. To account for this, a multiplier is needed, and is obtained via calibrations with known amounts of each species input to the mass spectrometer.

$$Corrected \ gas \ species \ (\%) = m * uncorrected \ gas \ species \ (\%)$$

Also, when measuring the partial pressure of a species the mass spectrometer never reads a true zero and therefore a constant c was added to the calibration equation.

$$Actual \ gas \ species \ (\%) = m * uncorrected \ gas \ species \ (\%) + c$$

The above equation corresponds to or fits the equation of a straight line with

$$m = slope \ of \ the \ line$$

$$c = intercept$$

69

A-2 Calibration curves

The actual, corrected percentage of the gas species was obtained with a two point calibration using data from upstream and downstream positions, where the exact concentrations of the species were known. The upstream was known based on the inlet concentrations and the outlet was known using a FTIR instrument that measured outlet concentrations.

A.2.1 Propylene

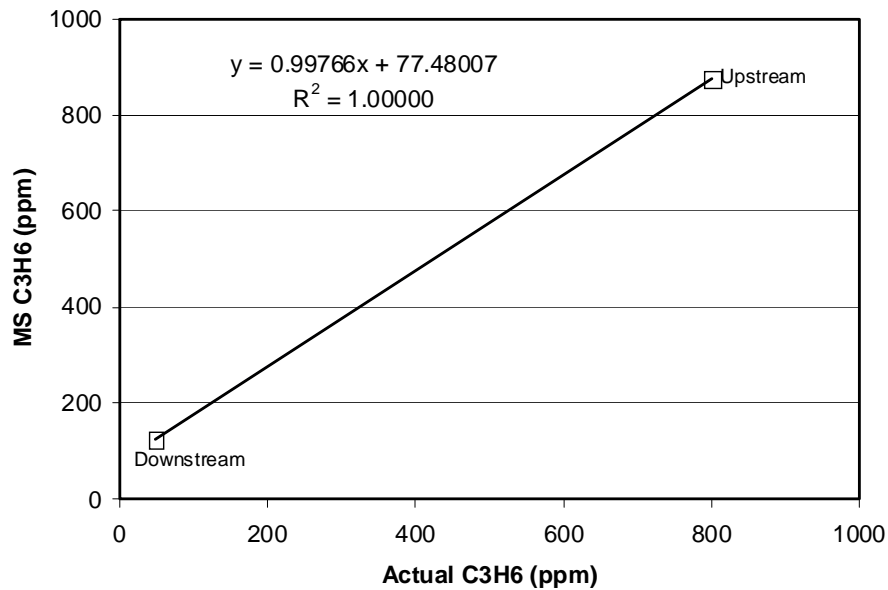Figure A-1 shows the calibration curve for C_3H_6 used for the steady state experiment at 248°C.

Figure A-1: Mass spectrometer calibration line for C_3H_6 during the steady state experiment at 248°C.

A.2.2 CO_2

As mentioned previously, the mass spectrometer cannot distinguish between CO and N_2 due to equivalent molecular masses, thus CO_2 is measured. At lower temperatures where there is no hydrocarbon oxidation observed, all the CO_2 comes from CO oxidation only. Thus, the calibration equation for the first 3 capillary positions during the steady state experiments at 248°C, where no hydrocarbon oxidation is observed is based on CO conversion according to the equation CO (in) – CO (out) = CO_2 (out). The calibration curve is shown in Figure A-2.

A similar procedure is followed to obtain the amount of CO_2 and the calibration curve for the steady state experiments at 128, 168 and 208°C.
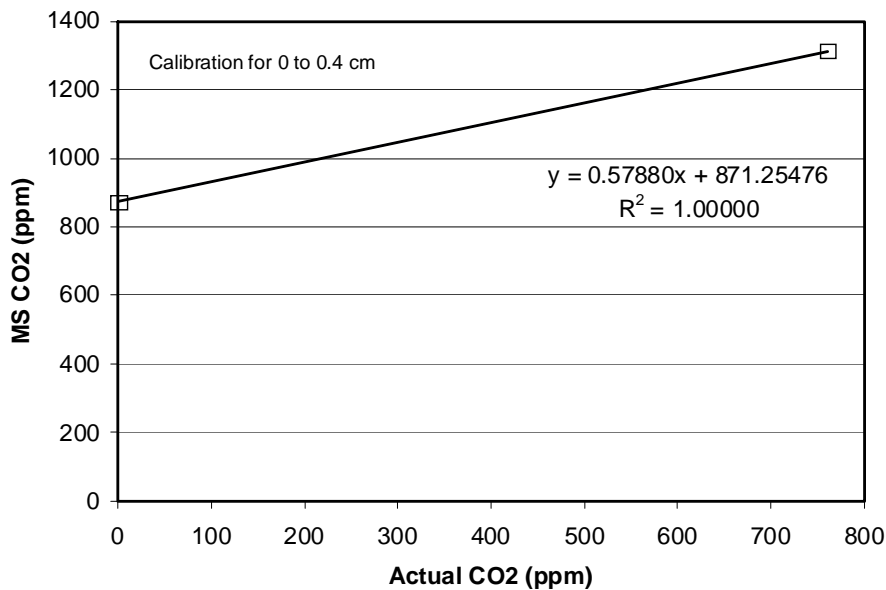

Figure A-2: Mass spectrometer calibration line for CO_2 for 0 to 0.4 cm from the inlet during the steady state experiment at 248°C.

At 248°C, hydrocarbon oxidation is observed beyond 0.4 cm from the inlet, which also contributes to the measured CO_2. The FTIR can detect CO_2, thus the ratio obtained from the mass spectrometer was compared to the FTIR readings to get the calibration curve shown in Figure A-3. This calibration procedure was used to obtain the actual concentration of CO_2 produced during the steady state experiment carried out at 290°C, as well as the temperature ramp experiments.
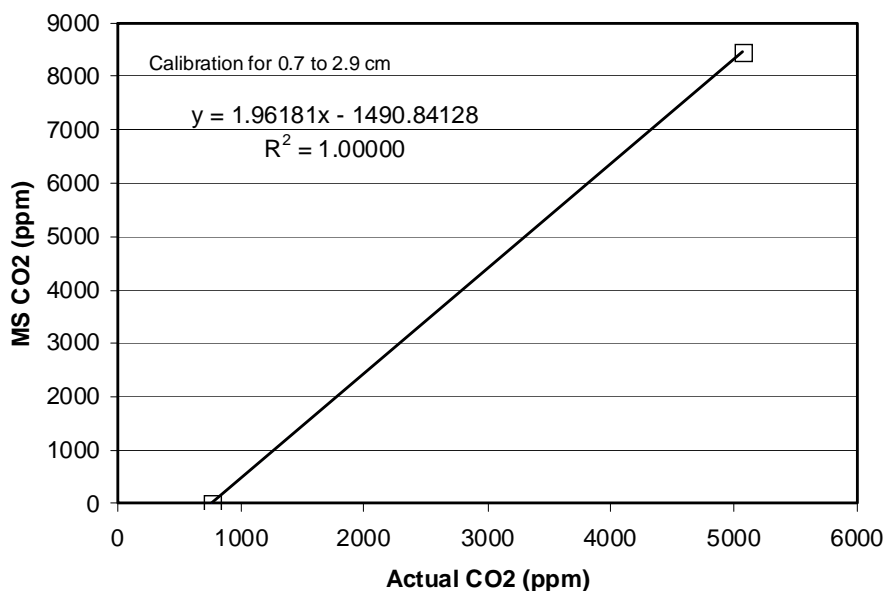

Figure A-3: Mass spectrometer calibration line for CO_2 for 0.7 to 2.9 cm from the inlet during the steady state experiment at 248°C.

Appendix B

B-1 Reproducibility checks- Effect of hydrocarbons on NO oxidation

To check the reproducibility of experiments conducted in Chapter 4, we use an experiment from Figure 4-5 as an example. From Figure B-1 we can see that the propylene oxidation experiments were reproducible, where the propylene concentration profiles for 0.075% O_2 are shown. The close match between the profiles visually indicates reproducibility.
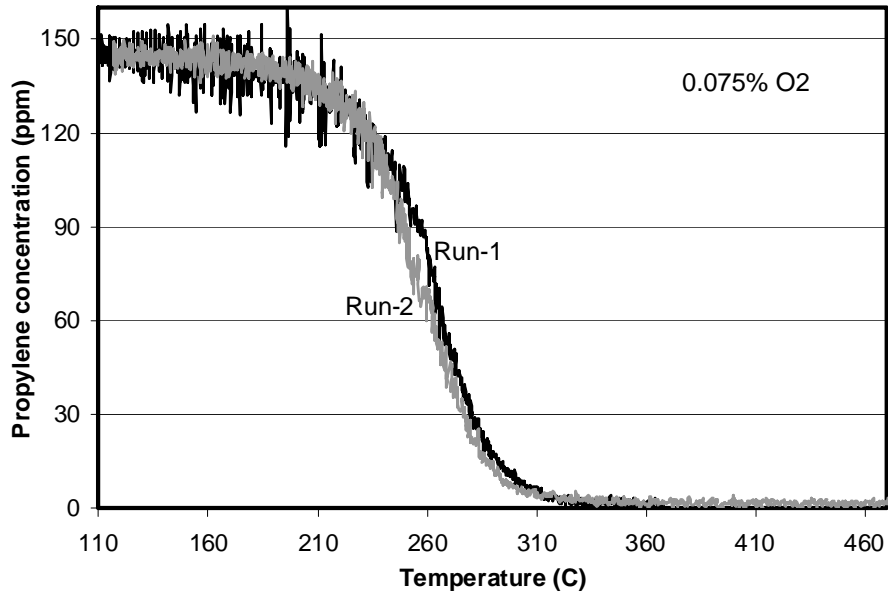
Figure B-1: Reproducibility check for C_3H_6 oxidation as a function of temperature and O_2 concentration. The feed stream contained 5% H_2O, 150 ppm C_3H_6, 0.075% O_2 and a balance of N_2.

B-2 Reproducibility checks - Spatial resolution of reactant species consumption

To check the reproducibility for experiments in Chapter 5, the high flow rate, temperature ramp experiment at 2.625 cm from the catalyst inlet was chosen as an example. Figures B-2 and B-3 show the reproducibility checks for propylene and dodecane conversions at 2.625 cm respectively. Once again the close match in profiles visually indicates reproducibility.
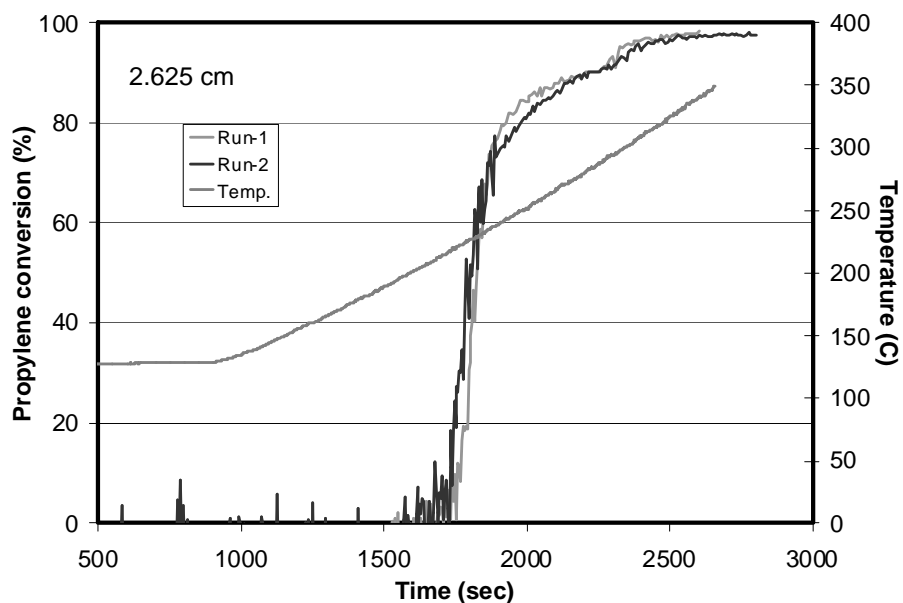
<u>Figure B-2</u>: Reproducibility check for C_3H_6 conversions as a function of time/temperature at 2.625 cm from the catalyst inlet and flow rate = 19.06 L/min.
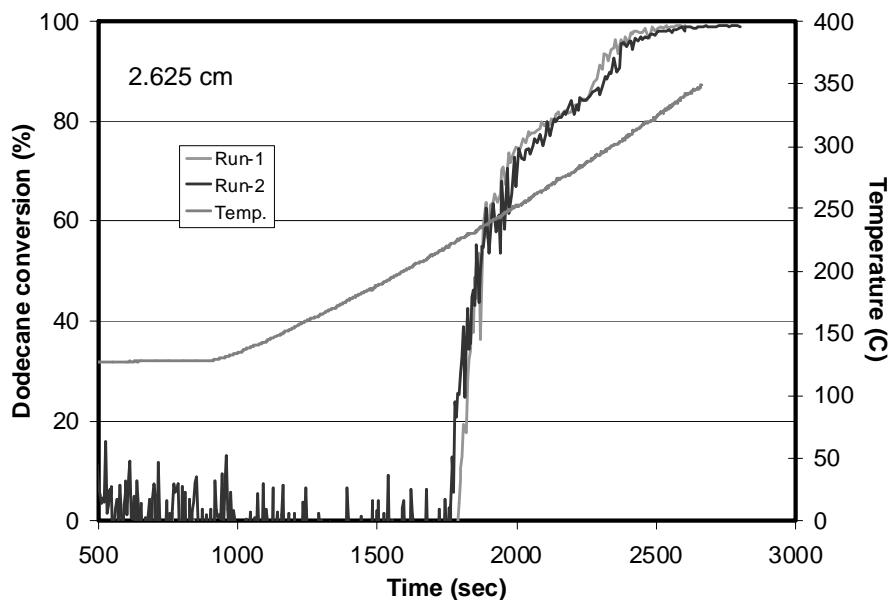

<u>Figure B-3</u>: Reproducibility check for $C_{12}H_{26}$ conversions as a function of time/temperature at 2.625 cm from the catalyst inlet and flow rate = 19.06 L/min.